



**HAL**  
open science

## Investigating Charge Transfer in Functionalized Mesoporous EISA-SnO<sub>2</sub> Films

Wael Hamd, Christel Laberty-Robert, François Lambert, Cyrille Costentin,  
Benoit Limoges, Veronique Balland

► **To cite this version:**

Wael Hamd, Christel Laberty-Robert, François Lambert, Cyrille Costentin, Benoit Limoges, et al..  
Investigating Charge Transfer in Functionalized Mesoporous EISA-SnO<sub>2</sub> Films. *Journal of Physical  
Chemistry C*, 2017, 121 (41), pp.23207-23217. 10.1021/acs.jpcc.7b07071 . hal-01614721

**HAL Id: hal-01614721**

**<https://hal.sorbonne-universite.fr/hal-01614721>**

Submitted on 11 Oct 2017

**HAL** is a multi-disciplinary open access archive for the deposit and dissemination of scientific research documents, whether they are published or not. The documents may come from teaching and research institutions in France or abroad, or from public or private research centers.

L'archive ouverte pluridisciplinaire **HAL**, est destinée au dépôt et à la diffusion de documents scientifiques de niveau recherche, publiés ou non, émanant des établissements d'enseignement et de recherche français ou étrangers, des laboratoires publics ou privés.

## Article

## Investigating Charge Transfer in Functionalized Mesoporous EISA-SnO Films

Wael Hamd, Christel Laberty-Robert, François Lambert,  
Cyrille Costentin, Benoit Limoges, and Veronique Balland*J. Phys. Chem. C*, **Just Accepted Manuscript** • DOI: 10.1021/acs.jpcc.7b07071 • Publication Date (Web): 25 Sep 2017Downloaded from <http://pubs.acs.org> on September 27, 2017

## Just Accepted

"Just Accepted" manuscripts have been peer-reviewed and accepted for publication. They are posted online prior to technical editing, formatting for publication and author proofing. The American Chemical Society provides "Just Accepted" as a free service to the research community to expedite the dissemination of scientific material as soon as possible after acceptance. "Just Accepted" manuscripts appear in full in PDF format accompanied by an HTML abstract. "Just Accepted" manuscripts have been fully peer reviewed, but should not be considered the official version of record. They are accessible to all readers and citable by the Digital Object Identifier (DOI®). "Just Accepted" is an optional service offered to authors. Therefore, the "Just Accepted" Web site may not include all articles that will be published in the journal. After a manuscript is technically edited and formatted, it will be removed from the "Just Accepted" Web site and published as an ASAP article. Note that technical editing may introduce minor changes to the manuscript text and/or graphics which could affect content, and all legal disclaimers and ethical guidelines that apply to the journal pertain. ACS cannot be held responsible for errors or consequences arising from the use of information contained in these "Just Accepted" manuscripts.



# Investigating Charge Transfer in Functionalized Mesoporous EISA-SnO<sub>2</sub> Films

Wael Hamd,<sup>†</sup> Christel Laberty-Robert,<sup>#</sup> François Lambert,<sup>§</sup> Cyrille Costentin,<sup>†</sup> Benoît Limoges<sup>†,\*</sup>  
and Véronique Balland<sup>†,\*</sup>

<sup>†</sup> *Laboratoire d'Electrochimie Moléculaire, UMR 7591 CNRS, Université Paris Diderot,  
Sorbonne Paris Cité, 15 rue Jean-Antoine de Baïf, F-75205 Paris Cedex 13, France*

<sup>#</sup> *Sorbonne Universités, UPMC Univ Paris 6, CNRS, Collège de France, Laboratoire de Chimie  
de la Matière Condensée de Paris, 4 place Jussieu, F-75005 Paris, France.*

<sup>§</sup> *Laboratoire des Biomolécules, UMR 7203 CNRS, UPMC Univ Paris 6, Ecole Normale  
Supérieure, 24 rue Lhomond, F-75005 Paris, France.*

1  
2  
3 ABSTRACT. Semiconductive transparent thin films of periodically-organized nanostructured  
4  
5 SnO<sub>2</sub> were prepared on flat conductive ITO substrates by evaporation-induced self-assembly  
6  
7 (EISA) under different dip-coating regimes and then functionalized by two redox-active  
8  
9 chromophores, i.e. the flavin mononucleotide (FMN) able to reversibly exchange 2 e<sup>-</sup> and 2 H<sup>+</sup>  
10  
11 and the [Os<sup>II</sup>(bpy)<sub>2</sub>(4,4'-CH<sub>2</sub>PO<sub>3</sub>H<sub>2</sub>-bpy)]<sup>2+</sup> complex (OsP) involving a fast and reversible one-  
12  
13 electron transfer. The redox behavior of these two chemisorbed chromophores was investigated  
14  
15 by cyclic voltammetry and cyclic voltabsorptometry. On account of the distinct formal potential  
16  
17 of the two redox chromophores relative to the position of the lower conduction band edge of  
18  
19 SnO<sub>2</sub>, the heterogeneous electron transfer was observed either reversible (FMN) or irreversible  
20  
21 (OsP). In the case of the OsP-functionalized SnO<sub>2</sub> electrode, quantitative analysis of the cyclic  
22  
23 voltabsorptograms was achieved within the framework of our previously proposed kinetic model  
24  
25 of charge transfer/transport in mesoporous semiconductive films (Renault *et al.*, *Phys. Chem.*  
26  
27 *Chem. Phys.* **2015**, *17*, 10592–607), allowing for direct comparison between EISA-TiO<sub>2</sub> and  
28  
29 EISA-SnO<sub>2</sub> electrodes. It is notably shown that the interfacial electron transfer between the  
30  
31 adsorbed redox chromophore and the SnO<sub>2</sub> interface is the rate-determining process under our  
32  
33 experimental conditions. It is additionally demonstrated that the electrons trapped in the low-  
34  
35 energy surface states of EISA-SnO<sub>2</sub> can directly participate to the interfacial electron transfer, a  
36  
37 behavior that strongly contrasts to that we had previously found at EISA-TiO<sub>2</sub> electrodes (i.e.,  
38  
39 wherein only electrons from the conduction band were involved in the interfacial electron  
40  
41 transfer).  
42  
43  
44  
45  
46  
47  
48  
49  
50  
51  
52  
53  
54  
55  
56  
57  
58  
59  
60

1  
2  
3 INTRODUCTION  
4  
5

6 Photoanodes based on nanoporous semiconductive films of SnO<sub>2</sub> are recognized as an  
7 alternative to the much more widely explored nanoporous films of TiO<sub>2</sub>, especially as part of  
8 photoelectrocatalytic cells (DSPECs) operating under sunlight irradiation.<sup>1,2</sup> Essential to the  
9 development of such photoanodes is the sensitization of the porous transparent semi-conductive  
10 metal oxide film by redox-active chromophores that adsorb visible light and promote fast  
11 electron injection into the conduction band of the semiconductor. The ensuing photo-oxidized  
12 chromophore can then be used either directly or indirectly (i.e., through the intermediate of a co-  
13 immobilized catalyst) to oxidize a substrate in solution (e.g., water in the case of a water-splitting  
14 DSPEC). The main advantage of SnO<sub>2</sub> over TiO<sub>2</sub> is its conduction band potential shifted ~0.4 V  
15 more positive than TiO<sub>2</sub>,<sup>3,4</sup> expanding thus the choice of redox-active chromophores that feature  
16 less reducing excited states and in turn higher ground-state oxidation potentials (which is  
17 beneficial to drive the oxidation of water in a water-splitting DSPEC or any other molecules  
18 difficult to oxidize in others photoelectrocatalytic applications).<sup>5-8</sup> Others advantages of SnO<sub>2</sub>  
19 rely on its wide band gap (~3.6 eV), therefore decreasing complications from direct band gap  
20 excitation and promoting long term stability under the harsh chemical conditions generally  
21 involved in DSPEC applications. This is also a n-type semiconductor that leads to faster electron  
22 transport characteristics than TiO<sub>2</sub>.<sup>9</sup> Such faster electron transport should theoretically favor the  
23 collection efficiency of photoinjected electrons at the expense of losses by interfacial charge  
24 transfer recombination. However, despite this, only poor device efficiencies have been reported  
25 to date with nanoporous SnO<sub>2</sub>-based photoanodes.<sup>2</sup>

26  
27  
28  
29  
30  
31  
32  
33  
34  
35  
36  
37  
38  
39  
40  
41  
42  
43  
44  
45  
46  
47  
48  
49  
50  
51  
52  
53  
54  
55  
56  
57  
58  
59  
60  
61  
62  
63  
64  
65  
66  
67  
68  
69  
70  
71  
72  
73  
74  
75  
76  
77  
78  
79  
80  
81  
82  
83  
84  
85  
86  
87  
88  
89  
90  
91  
92  
93  
94  
95  
96  
97  
98  
99  
100  
101  
102  
103  
104  
105  
106  
107  
108  
109  
110  
111  
112  
113  
114  
115  
116  
117  
118  
119  
120  
121  
122  
123  
124  
125  
126  
127  
128  
129  
130  
131  
132  
133  
134  
135  
136  
137  
138  
139  
140  
141  
142  
143  
144  
145  
146  
147  
148  
149  
150  
151  
152  
153  
154  
155  
156  
157  
158  
159  
160  
161  
162  
163  
164  
165  
166  
167  
168  
169  
170  
171  
172  
173  
174  
175  
176  
177  
178  
179  
180  
181  
182  
183  
184  
185  
186  
187  
188  
189  
190  
191  
192  
193  
194  
195  
196  
197  
198  
199  
200  
201  
202  
203  
204  
205  
206  
207  
208  
209  
210  
211  
212  
213  
214  
215  
216  
217  
218  
219  
220  
221  
222  
223  
224  
225  
226  
227  
228  
229  
230  
231  
232  
233  
234  
235  
236  
237  
238  
239  
240  
241  
242  
243  
244  
245  
246  
247  
248  
249  
250  
251  
252  
253  
254  
255  
256  
257  
258  
259  
260  
261  
262  
263  
264  
265  
266  
267  
268  
269  
270  
271  
272  
273  
274  
275  
276  
277  
278  
279  
280  
281  
282  
283  
284  
285  
286  
287  
288  
289  
290  
291  
292  
293  
294  
295  
296  
297  
298  
299  
300  
301  
302  
303  
304  
305  
306  
307  
308  
309  
310  
311  
312  
313  
314  
315  
316  
317  
318  
319  
320  
321  
322  
323  
324  
325  
326  
327  
328  
329  
330  
331  
332  
333  
334  
335  
336  
337  
338  
339  
340  
341  
342  
343  
344  
345  
346  
347  
348  
349  
350  
351  
352  
353  
354  
355  
356  
357  
358  
359  
360  
361  
362  
363  
364  
365  
366  
367  
368  
369  
370  
371  
372  
373  
374  
375  
376  
377  
378  
379  
380  
381  
382  
383  
384  
385  
386  
387  
388  
389  
390  
391  
392  
393  
394  
395  
396  
397  
398  
399  
400  
401  
402  
403  
404  
405  
406  
407  
408  
409  
410  
411  
412  
413  
414  
415  
416  
417  
418  
419  
420  
421  
422  
423  
424  
425  
426  
427  
428  
429  
430  
431  
432  
433  
434  
435  
436  
437  
438  
439  
440  
441  
442  
443  
444  
445  
446  
447  
448  
449  
450  
451  
452  
453  
454  
455  
456  
457  
458  
459  
460  
461  
462  
463  
464  
465  
466  
467  
468  
469  
470  
471  
472  
473  
474  
475  
476  
477  
478  
479  
480  
481  
482  
483  
484  
485  
486  
487  
488  
489  
490  
491  
492  
493  
494  
495  
496  
497  
498  
499  
500  
501  
502  
503  
504  
505  
506  
507  
508  
509  
510  
511  
512  
513  
514  
515  
516  
517  
518  
519  
520  
521  
522  
523  
524  
525  
526  
527  
528  
529  
530  
531  
532  
533  
534  
535  
536  
537  
538  
539  
540  
541  
542  
543  
544  
545  
546  
547  
548  
549  
550  
551  
552  
553  
554  
555  
556  
557  
558  
559  
560  
561  
562  
563  
564  
565  
566  
567  
568  
569  
570  
571  
572  
573  
574  
575  
576  
577  
578  
579  
580  
581  
582  
583  
584  
585  
586  
587  
588  
589  
590  
591  
592  
593  
594  
595  
596  
597  
598  
599  
600  
601  
602  
603  
604  
605  
606  
607  
608  
609  
610  
611  
612  
613  
614  
615  
616  
617  
618  
619  
620  
621  
622  
623  
624  
625  
626  
627  
628  
629  
630  
631  
632  
633  
634  
635  
636  
637  
638  
639  
640  
641  
642  
643  
644  
645  
646  
647  
648  
649  
650  
651  
652  
653  
654  
655  
656  
657  
658  
659  
660  
661  
662  
663  
664  
665  
666  
667  
668  
669  
670  
671  
672  
673  
674  
675  
676  
677  
678  
679  
680  
681  
682  
683  
684  
685  
686  
687  
688  
689  
690  
691  
692  
693  
694  
695  
696  
697  
698  
699  
700  
701  
702  
703  
704  
705  
706  
707  
708  
709  
710  
711  
712  
713  
714  
715  
716  
717  
718  
719  
720  
721  
722  
723  
724  
725  
726  
727  
728  
729  
730  
731  
732  
733  
734  
735  
736  
737  
738  
739  
740  
741  
742  
743  
744  
745  
746  
747  
748  
749  
750  
751  
752  
753  
754  
755  
756  
757  
758  
759  
760  
761  
762  
763  
764  
765  
766  
767  
768  
769  
770  
771  
772  
773  
774  
775  
776  
777  
778  
779  
780  
781  
782  
783  
784  
785  
786  
787  
788  
789  
790  
791  
792  
793  
794  
795  
796  
797  
798  
799  
800  
801  
802  
803  
804  
805  
806  
807  
808  
809  
810  
811  
812  
813  
814  
815  
816  
817  
818  
819  
820  
821  
822  
823  
824  
825  
826  
827  
828  
829  
830  
831  
832  
833  
834  
835  
836  
837  
838  
839  
840  
841  
842  
843  
844  
845  
846  
847  
848  
849  
850  
851  
852  
853  
854  
855  
856  
857  
858  
859  
860  
861  
862  
863  
864  
865  
866  
867  
868  
869  
870  
871  
872  
873  
874  
875  
876  
877  
878  
879  
880  
881  
882  
883  
884  
885  
886  
887  
888  
889  
890  
891  
892  
893  
894  
895  
896  
897  
898  
899  
900  
901  
902  
903  
904  
905  
906  
907  
908  
909  
910  
911  
912  
913  
914  
915  
916  
917  
918  
919  
920  
921  
922  
923  
924  
925  
926  
927  
928  
929  
930  
931  
932  
933  
934  
935  
936  
937  
938  
939  
940  
941  
942  
943  
944  
945  
946  
947  
948  
949  
950  
951  
952  
953  
954  
955  
956  
957  
958  
959  
960  
961  
962  
963  
964  
965  
966  
967  
968  
969  
970  
971  
972  
973  
974  
975  
976  
977  
978  
979  
980  
981  
982  
983  
984  
985  
986  
987  
988  
989  
990  
991  
992  
993  
994  
995  
996  
997  
998  
999  
1000

Better understanding the factors limiting the performance of nanoporous SnO<sub>2</sub> photoanodes  
compared to those based on other nanostructured metal oxides is therefore key to better assess

1  
2  
3 the actual potentialities offered by this material in DSPEC applications. These factors include not  
4  
5 only the dynamics of electron transport by diffusion throughout the mesoporous metal-oxide  
6  
7 network, but also the interfacial electron transfer kinetics associated both to the photoinjection of  
8  
9 electrons in SnO<sub>2</sub> and to the back electron transfer (BET) resulting from charge recombination  
10  
11 between electrons injected in SnO<sub>2</sub> and the oxidized dye or species present in solution. Several  
12  
13 studies have already addressed the electron injection dynamics in SnO<sub>2</sub> from diverse  
14  
15 photoexcited redox dyes adsorbed in nanocrystalline films.<sup>4,9-13</sup> Electron injection rates were  
16  
17 shown to proceed within the pico- to nanosecond range, which is ~1 order of magnitude lower  
18  
19 than for TiO<sub>2</sub>. This lower injection rate has been attributed to a lower density of states in the  
20  
21 conduction band of SnO<sub>2</sub> compared to TiO<sub>2</sub> (the available density of states is almost two orders  
22  
23 of magnitude higher in TiO<sub>2</sub> than in SnO<sub>2</sub>).<sup>14</sup> Interfacial charge recombination in dye-sensitized  
24  
25 nanoporous SnO<sub>2</sub> films have also been the subject of several studies.<sup>4,15,16</sup> These BET reactions  
26  
27 are undesired since they compete with the substrate oxidation in solution, contributing thus to the  
28  
29 loss of DSPEC performance. Consequently, minimizing the interfacial charge recombination is  
30  
31 key for developing efficient DSPEC devices. BET rates in dye-sensitized SnO<sub>2</sub> or TiO<sub>2</sub> films  
32  
33 were found to occur within the micro- to millisecond time scale, depending on the nature of the  
34  
35 excited dye and electrolyte solution. BET rates were found significantly higher in SnO<sub>2</sub> than in  
36  
37 TiO<sub>2</sub> (roughly 2 orders of magnitude faster in SnO<sub>2</sub> than TiO<sub>2</sub> when working in organic media  
38  
39 and only 2-3 fold faster when operating in an aqueous acidic electrolyte), a behavior that was  
40  
41 attributed to differences in the energy distribution and density of intra-band-gap states (i.e.,  
42  
43 including bulk trap states and surface states).<sup>4,15,16</sup> Faster electron diffusion in SnO<sub>2</sub> was indeed  
44  
45 attributed to a lower bulk trap density,<sup>4</sup> while the role of surface states in the recombination  
46  
47 process was evidenced from atomic layer deposition of conformal thin passivating coatings of  
48  
49  
50  
51  
52  
53  
54  
55  
56  
57  
58  
59  
60

1  
2  
3 Al<sub>2</sub>O<sub>3</sub> or TiO<sub>2</sub> on the surface of mesoporous SnO<sub>2</sub> films, resulting thus in a decrease of the  
4  
5 recombination rates.<sup>17,18</sup>  
6  
7

8 In an attempt to better understand the key factors governing the BET reactions in  
9  
10 semiconductive nanostructured SnO<sub>2</sub> films, we investigate here by real-time cyclic  
11  
12 voltabsorptometry the redox behavior of two different redox-active chromophores that are  
13  
14 strongly chemisorbed on the surface of highly-ordered mesoporous thin films of SnO<sub>2</sub>. The  
15  
16 methodology used for extracting the key information is similar to the one we have recently  
17  
18 developed for analyzing the interfacial electron transfer parameters in mesoporous films of TiO<sub>2</sub>  
19  
20 functionalized by iron-porphyrin-based compounds.<sup>19</sup> The SnO<sub>2</sub> films are prepared by  
21  
22 evaporation-induced self-assembly (EISA), a sol-gel surfactant-templated synthetic method  
23  
24 which leads to the formation of highly periodically-organized nanoporous metal oxides thin films  
25  
26 on a flat solid substrate (i.e. a transparent conductive ITO electrode in the present case).<sup>20</sup> The  
27  
28 main interests of these mesoscopic films are their well-defined porosity, well-controlled 3D  
29  
30 organization, high specific surface area, and relatively robust inorganic structure made of thick  
31  
32 semicrystalline walls. These specific properties are not only advantageous for the development  
33  
34 of efficient DSPEC devices but also useful for fundamental studies whose objective is to  
35  
36 quantitatively analyze the different modes of charge transfer/transport in these highly-organized  
37  
38 films. Still, only a few papers report on the preparation of crystalline mesoporous SnO<sub>2</sub> films by  
39  
40 EISA.<sup>21</sup> This can be explained by the difficulties encountered during the crystallization process  
41  
42 at high temperature, difficulties that however can be overwhelmed with amphiphilic block-  
43  
44 copolymers organic templates (“KLE” type) on account of their better thermal stabilities than  
45  
46 pluronic templates.<sup>21</sup> In the present study, we demonstrate that highly nanoporous crystalline  
47  
48 EISA-SnO<sub>2</sub> thin films can be obtained from commercial block copolymers of polyisobutylene-  
49  
50  
51  
52  
53  
54  
55  
56  
57  
58  
59  
60

1  
2  
3 polyethylene oxide (PIB-*b*-PEO). Additionally, the film thickness (~250 nm) is shown to be  
4  
5 maximized by adjusting the one-step dip-coating process at very low withdrawal speeds (i.e.,  
6  
7 draining regime).<sup>22</sup> The resulting SnO<sub>2</sub> films are chemically functionalized by Flavin  
8  
9 mononucleotide (FMN, able to reversibly exchange 2 e<sup>-</sup> and 2 H<sup>+</sup>) or the [Os<sup>II</sup>(bpy)<sub>2</sub>(4,4'-  
10  
11 CH<sub>2</sub>PO<sub>3</sub>H<sub>2</sub>-bpy)]<sup>2+</sup> complex (OsP, a one-electron transfer complex) through chemisorption of  
12  
13 their phosphate/phosphonate anchoring group and characterized by cyclic voltabsorptometry.  
14  
15 On account of the distinct formal potential of the two redox chromophores relative to the  
16  
17 position of the lower conduction band edge of SnO<sub>2</sub>, the heterogeneous electron transfer is  
18  
19 shown either reversible or irreversible. In the case of the irreversible charge transfer with the  
20  
21 OsP-functionalized EISA-SnO<sub>2</sub> electrode, it is found that electrons trapped in the low-energy  
22  
23 surface states of EISA-SnO<sub>2</sub> can directly participate to the interfacial electron transfer. This  
24  
25 observation contrasts to our previous results with mesoporous EISA-TiO<sub>2</sub> films wherein the  
26  
27 interfacial electron transfer to an absorbed redox compound was shown to proceed exclusively  
28  
29 through the extended conduction band states.<sup>19</sup> The present results confirm that multiple  
30  
31 interfacial recombination pathways coexist in mesoporous SnO<sub>2</sub> electrodes and that the localized  
32  
33 low-energy surface states contribute significantly to the undesirable charge recombination, a  
34  
35 process that has been previously suggested to predominate in mesoscopic SnO<sub>2</sub> films than TiO<sub>2</sub>  
36  
37 films.<sup>17,18</sup>  
38  
39  
40  
41  
42  
43  
44  
45  
46  
47  
48  
49  
50  
51  
52  
53  
54  
55  
56  
57  
58  
59  
60



## EXPERIMENTAL DETAILS

**Chemicals.** Tin tetrachloride (99%), and solvents were purchased from Sigma Aldrich, polyisobutylene-polyethyleneoxide (PIB-b-PEO; reference P4973-ibEO: MWPIB= 7000 g·mol<sup>-1</sup>, MWPEO ¼ 8500 g·mol<sup>-1</sup>) was purchased from Polymer Source. All the chemical reagents used in the experiments were obtained from commercial sources as guaranteed-grade reagents and used without further purification. The osmium complex [Os(bpy)<sub>2</sub>(4,4'-(CH<sub>2</sub>PO<sub>3</sub>H<sub>2</sub>)bpy)]Cl<sub>2</sub> (OsP) was prepared according to a procedure described for Ruthenium.<sup>23</sup> The product was characterized by cyclic voltammetry in a Hepes Buffer solution (pH 7) by a single reversible wave centered at 0.6 V vs Ag/AgCl. Planar ITO-glass substrates were purchased from SOLEMS.

**Synthesis of templated SnO<sub>2</sub>.** 175 mg of PIB-b-PEO was dissolved in a mixture of 5.6 g EtOH and 0.4 g H<sub>2</sub>O by careful heating to 70 °C for 1 hour. After cooling for several minutes, 1.2 g of SnCl<sub>4</sub> was added dropwise. Then, the solution was stirred for 48 h. The resulting clear solution was dip-coated at ambient temperature on commercial ITO-coated glass substrates to produce thin films.

All films were prepared using a new generation homemade dip-coater (from SolGelWay). Films were deposited at a relatively low humidity (20%) at withdrawal speeds ranging from 0.01 to 5 mm s<sup>-1</sup> and at room temperature. The whole dip-coater was isolated from natural vibration and external convection so as to prevent the formation of horizontal strips (thickness non-uniformity) associated with the fluctuation of the solution surface that creates meniscus instability. In the present investigation, the same container was used to make sure the meniscus shape was similar for each experiment and also to diminish the potential fluctuation of the meniscus height during deposition due to vibration-induced surface instability. These controls are necessary for ultralow withdrawal speeds. After complete drying in air, hybrid films were

1  
2  
3 directly transferred underneath a curing IR lamp to be thermally treated at 500 °C in air for 1  
4  
5 hour to decompose the organic parts, to complete the inorganic condensation and to induce the  
6  
7 crystallization of SnO<sub>2</sub>.  
8  
9

10 **Ellipsometry.** The thickness ( $h$ ) and the refractive index ( $n$ ) of optical films were measured by  
11  
12 ellipsometry under UV-visible light at 70° variable angles. Thermal ellipsometry analysis was  
13  
14 performed between 80 and 500 °C to determine the most adequate heat-treatment for the  
15  
16 transformation of the hybrid organic inorganic film into a crystalline mesoporous films  
17  
18 Measurements were performed in the wavelength range of 400 to 900 nm, using a covered  
19  
20 heating unit connected and monitored by a programmable temperature regulator. The  
21  
22 thermocouple regulator was directly in contact with the sample.  
23  
24  
25  
26

27 After dip-coating, the as-prepared hybrid organic–inorganic films deposited onto silicon wafer  
28  
29 were heated at 80 °C for 10 minutes inside the covered heating unit, just before analysis  
30  
31 measurements. Data analysis was performed with Wvase32 software, where ellipsometric data  
32  
33  $\tan(C)$  and  $\cos(D)$  were fitted using a single Lorentz oscillator layer model with one oscillator  
34  
35 with center energy fixed at zero and other with free center energy in the UV-visible domain. The  
36  
37 thickness ( $h$ ), the real ( $n$ ) and imaginary ( $k$ ) parts of the complex refractive index of the films  
38  
39 were also evaluated.  
40  
41  
42

43 **Environmental ellipsometry porosimetry (EEP).** Investigations were conducted at room  
44  
45 temperature (25°C) using the adsorption–desorption isotherm of water analyzed with an isotropic  
46  
47 inorganic pore contraction model (IIC) and a modified Kelvin equation for ellipsoidal pores. Pore  
48  
49 volume and adsorbed water content were estimated through the Bruggeman Effective Medium  
50  
51 Approximation using the optical properties of the pure media (ZnO, SiO<sub>2</sub>, air and H<sub>2</sub>O). The  
52  
53 ellipsometer was fitted with a small, variable humidity flow chamber (SOPRA) flushed with 2.5  
54  
55  
56  
57  
58  
59  
60

1  
2  
3 L of air per min. The humidity was adjusted using a mass flow controller and monitored using a  
4  
5 relative humidity probe held in the environmental chamber.  
6  
7

8 **SEM FEG, EDX.** The microstructures of the films obtained at different withdraw speed were  
9  
10 observed by Field Emission (FE) Gun Scanning Electron Microscopy (FE-SEM, Hitachi). The  
11  
12 chemical compositional analysis of the films was performed by Energy Dispersive X-ray  
13  
14 spectroscopy.  
15  
16

17  
18 **XRD.** The structure of the mesoporous SnO<sub>2</sub> films was determined using a prototype X-ray  
19  
20 diffractometer equipped with a curved position sensitive detector (120°) from Inel. A fixed-  
21  
22 incidence monochromatic CoK $\alpha$  impinging parallel beam is obtained by reflection on a flat  
23  
24 Ge(111) crystal. Cobalt radiation was used instead of more usual copper radiation to avoid  
25  
26 sample fluorescence. The beam cross-section was 0.05 $\times$ 6 mm<sup>2</sup>, producing a rectangular 3 $\times$ 6 mm<sup>2</sup>  
27  
28 beam footprint on the sample at a fixed incidence of 1°. At this incidence, the attenuation length  
29  
30 inside the hematite sample is about 0.7 mm. The grazing incidence diffraction patterns ( $0 < 2\theta <$   
31  
32  $120^\circ$ ,  $\Delta 2\theta = 0.015^\circ$ ,  $\alpha = 1^\circ$ ) were refined using the Rietveld software XND. The broadening  
33  
34 components related to finite crystallite size and microstrain were determined after taking into  
35  
36 account the specific corrections for the instrumental broadening related to the grazing incidence  
37  
38 setup.  
39  
40  
41  
42  
43

44 **Electrode Functionalization.** Adsorption of the water-soluble redox probes (FMN or OsP)  
45  
46 into the highly ordered mesoporous structure of SnO<sub>2</sub> thin films (~250-nm thick) was achieved at  
47  
48 room temperature by immersing the mesoporous SnO<sub>2</sub>-coated ITO glass plates in a 1 mM milli-  
49  
50 Q aqueous solution (pH ~5) of each redox probe for few hours (> 2 hours). After adsorption, the  
51  
52 modified electrodes were carefully rinsed with milli-Q water and soaked for 1 hour in the buffer  
53  
54  
55  
56  
57  
58  
59  
60

1  
2  
3 solution (50 mM Hepes, 300 mM KCl, pH 7.0) to desorb low affinity fractions of the redox  
4 probes prior characterization by spectroelectrochemistry.  
5  
6

7  
8 **Spectroelectrochemistry.** For spectroelectrochemical experiments, a TORUS UV-visible  
9 diode-array spectrophotometer (Ocean Optics), equipped with optical fibers and a balanced  
10 deuterium tungsten source (Micropack), was coupled to an Autolab potentiostat PGSTAT 12  
11 (EcoChemie) interfaced to a PC computer (GPES software). Both instruments were synchronized  
12 through an input trigger signal generated from the potentiostat, allowing thus to simultaneously  
13 recorded the change of optical absorbance during a chronoamperometric or a cyclic voltammetric  
14 scan. The spectroelectrochemical measurements were performed in a home-made one-  
15 compartment three-electrode cell. The SnO<sub>2</sub>-film-coated ITO glass substrate was used as the  
16 working electrode, whereas a platinum wire and Ag/AgCl electrode in 3 M KCl were used as  
17 counter and reference electrodes, respectively (i.e., +0.20 V vs. NHE at 20°C). All potentials in  
18 the work were quoted to this reference electrode. The working electrode was prepared from a  
19 small rectangular piece of 0.8 × 3.5 cm cut from a SnO<sub>2</sub>-film-coated ITO glass plate. A working  
20 area of 0.30 ± 0.05 cm<sup>2</sup> was delimited from one extremity of the rectangular piece by depositing  
21 an insulating layer of varnish.  
22  
23  
24  
25  
26  
27  
28  
29  
30  
31  
32  
33  
34  
35  
36  
37  
38  
39

40  
41 The three electrodes were inserted in a 1-cm path length quartz cell through a silicon cap that  
42 hermetically closes the cell. An additional Tygon tube was introduced for degassing. The  
43 spectroelectrochemical cell was filled with 1.5 mL buffer and was thoroughly freed of air by  
44 bubbling with argon prior to the experiments. During the experiments, argon was continuously  
45 flowed over the solution in order to maintain the anaerobic environment and the cell was  
46 thermostated to 20°C using a Peltier-controlled cuvette holder (Quantum Northwest). All  
47  
48  
49  
50  
51  
52  
53  
54  
55  
56  
57  
58  
59  
60

1  
2  
3 experiments were carried out in an aqueous buffer of 50 mM Hepes (pH 7 and pH 8.5) or 50 mM  
4  
5 MES (pH 5 and pH 6), in the presence of 300 mM KCl.  
6  
7  
8  
9

## 10 RESULTS AND DISCUSSION

### 14 Preparation of the EISA-SnO<sub>2</sub> thin films.

16  
17 The mesoporous SnO<sub>2</sub> films were synthesized onto a flat conductive ITO-coated glass  
18  
19 substrate by a template-directed sol-gel synthesis coupled with a one-step dip-coating process.  
20  
21 Different withdrawal speeds were used for the dip-coating deposition allowing different  
22  
23 deposition regimes, i.e. the draining regime at high-speed values ( $> 1 \text{ mm}\cdot\text{s}^{-1}$ ) and the capillary  
24  
25 regime at speeds below  $0.1 \text{ mm}\cdot\text{s}^{-1}$ . The later allows for SnO<sub>2</sub> films characterized by a larger  
26  
27 thickness and thus a higher specific surface area enhancement.<sup>22</sup>  
28  
29  
30  
31

32 For all deposition regimes, dip-coating of the precursor sol resulted in an initial hybrid  
33  
34 transparent and homogeneous amorphous film, as indicated by the X-ray diffraction patterns.  
35  
36 High temperature annealing of the hybrid organic-inorganic films is then required to obtain a  
37  
38 crystalline material with an open porosity network. We have investigated the thermal behavior of  
39  
40 the hybrid organic-inorganic SnO<sub>2</sub> films in the draining regime by thermoellipsometry in order  
41  
42 to propose the adequate heat-treatment that (i) keeps the organization of pores defined by the  
43  
44 organic template in the hybrid organic-inorganic films and (ii) allows for a good crystallization  
45  
46 of the inorganic walls. The variation of SnO<sub>2</sub> film thickness as a function of temperature is  
47  
48 reported in Figure S1. The derivative curve exhibits three main peaks related to various  
49  
50 phenomena. The first peak at low temperature ( $\sim 120^\circ\text{C}$ ) corresponds to a thickness decrease  
51  
52 resulting from the evaporation of residual solvents such as H<sub>2</sub>O and EtOH. Between  $220^\circ\text{C}$  and  
53  
54  
55  
56  
57  
58  
59  
60

1  
2  
3 250 °C, variations of both thickness and refractive index are observed. It corresponds to the  
4 decomposition of PEO and PIB blocks to CO and CO<sub>2</sub> gases. Between 400 °C and 450 °C, the  
5  
6 low decrease of the thickness with temperature can be attributed to the crystallization of SnO<sub>2</sub>  
7  
8 nanocrystallites (by a nucleation and growth process). XRD peaks are characteristic of  
9  
10 cassiterite, a crystalline morphology identified on the X-ray diffraction patterns of 500 °C  
11  
12 calcined films. The decomposition of the different blocks thus occurs prior to the crystallization  
13  
14 of SnO<sub>2</sub> at around 450 °C. But, the final refractive index following this heat treatment is quite  
15  
16 high compared to those obtained by flash treatment at 500 °C, indicating the formation of the  
17  
18 porous network. Note that flash annealing induces an important inorganic growth leading to the  
19  
20 collapse of the pore structure. Accordingly, a thermal treatment at 500 °C in air for 1 hour was  
21  
22 required to form a nanostructured, mesoporous film of SnO<sub>2</sub> with a well-defined and highly  
23  
24 accessible porous network, allowing fast diffusion of chemicals.  
25  
26  
27  
28  
29  
30

### 31 **Physical characterization of the EISA-SnO<sub>2</sub> thin films.**

32  
33  
34  
35 The thickness of single-dip-coated mesoporous films, heat-treated at 500 °C, has been  
36  
37 evaluated by FE-SEM analyses and the value is comparable to that estimated by ellipsometry,  
38  
39 within the experimental errors (Table 1). Top-down and cross-section images show highly  
40  
41 porous and uniform heat-treated films (Figure 1). As expected, a much higher film thickness of  
42  
43 ca. 250 nm could be obtained in the capillary regime (withdrawal speed of 0.01 mm·s<sup>-1</sup>) than in  
44  
45 the draining regime wherein the maximum film thickness reached was only 100 nm (at a  
46  
47 withdrawal speed of 5 mm·s<sup>-1</sup>). For the larger film, the cross-section image shows ellipsoidal  
48  
49 pores which is attributed to a small contraction of the film during calcination / crystallization.  
50  
51  
52

53  
54 The composition of the nanostructured SnO<sub>2</sub> films was determined by EDX analyses (Figure  
55  
56 S2). We found that the principal element (Sn) was homogeneously distributed within the film.  
57  
58  
59  
60

1  
2  
3 We also denote the existence of (In) and (Si,Na) elements from the underlying ITO-glass  
4 substrate.  
5  
6

7  
8 The porosity of the EISA-SnO<sub>2</sub> films was analyzed by ellipsometric porosimetry. A similar  
9 behavior was observed for the 100- and 250-nm thick SnO<sub>2</sub> films prepared at 5 and 0.01 mm·s<sup>-1</sup>,  
10 respectively. The water adsorption/desorption isotherm is shown in Figure S3, and the  
11 corresponding pore size distribution plots calculated from both adsorption and desorption  
12 branches are given in Figure 1. Firstly, as expected from the very low refractive index ( $n = 1.22$ ),  
13 the accessible porosity is very high since one found 65-70% in total volume. This value was  
14 obtained based on the Bruggeman Effective Medium Approximation (BEMA), using  $n = 2$  at 700  
15 nm for the theoretical refractive index for crystalline bulk SnO<sub>2</sub>. The adsorption and desorption  
16 curves are almost overlapping over the humidity range, which suggests that the porosity is highly  
17 accessible, as one would expect from a 3D fully interconnected void network. Such an hysteresis  
18 suggests absence of restrictions, or presence of wide ones, which would then imply that pores are  
19 close to interconnected channels or open tubes.<sup>24,25</sup> Assuming so, and using the 27° (measured  
20 value) as the water contact angle on SnO<sub>2</sub> surface model in the Kelvin equation, one obtains a  
21 pore size distribution centered at ~30 nm based on the adsorption branch and at ~20nm based on  
22 the desorption branch (Table 1), although with a larger distribution of pore sizes for the thicker  
23 film. Such values are in good agreement with SEM microscopy observation.  
24  
25  
26  
27  
28  
29  
30  
31  
32  
33  
34  
35  
36  
37  
38  
39  
40  
41  
42  
43  
44  
45

#### 46 **Electrochemical characterization of the EISA-SnO<sub>2</sub> films**

47  
48

49 The electrochemical behavior of the 100- and 250-nm thick EISA-SnO<sub>2</sub> films was investigated  
50 by cyclic voltammetry in a buffered aqueous solution at pH 7 (in the presence of 0.3 M KCl). As  
51 shown on the cyclic voltammograms (CVs) in Figure 2, the capacitive current density recorded  
52 at  $E > 0.2$  V (vs. Ag/AgCl) remains low and independent of the applied potential. In this  
53  
54  
55  
56  
57  
58  
59  
60

1  
2  
3 potential window, the SnO<sub>2</sub> film behaves as an insulating porous layer as the applied potential  
4 remains much more positive than the conduction band potential of SnO<sub>2</sub>, the latter being  
5 estimated as  $E_{CB} = -0.39$  V at pH = 7.0 according to the following relationship (in V vs.  
6 Ag/AgCl):<sup>3</sup>  
7  
8  
9  
10

$$11 \quad E_{CB} = 0.02 - 0.059 \text{ pH} \quad (1)$$

12  
13  
14  
15  
16  
17 As a result, at potentials  $E > 0.2$  V, the observed background current only arises from the  
18 electrical double-layer charging capacitance of the underlying exposed conductive ITO substrate.  
19  
20 As the potential is progressively downshifted to cathodic values, *i.e.* for  $E < 0.2$  V, the cyclic  
21 voltammograms (CVs) are characterized by an exponential increase of the current density which  
22 varies proportionally to the scan rate (Figure 2). This behavior is analogous to that previously  
23 described for electrodes prepared from randomly sintered SnO<sub>2</sub> nanoparticles.<sup>16</sup> This is also  
24 similar to that reported for mesoporous TiO<sub>2</sub> electrodes prepared either from randomly sintered  
25 nanoparticles or EISA, except that with this metal oxide the exponential growth of current occurs  
26 at significantly lower potential values ( $\sim 0.4$  V more negative) at the same pH.<sup>19,26,27</sup> The  
27 exponential increase of current as the applied potential is downshifted toward the conduction  
28 band potential of SnO<sub>2</sub> is characteristic of the progressive filling of electronic states present in  
29 the semi-conductive mesoporous material (*i.e.*, the filling of bulk or surface localized states that  
30 are distributed in the sub-bandgap region of SnO<sub>2</sub> and the filling of extended conduction band  
31 states when the potential is raised close to  $E_{CB}$ ). This current transition corresponds thus to the  
32 chemical capacitive charging current resulting from the exponential growth of conductivity  
33 within the semiconductive mesoporous SnO<sub>2</sub> film. This is finally only when the applied potential  
34 is sufficiently lower than the conduction band potential (*i.e.*, at  $E < E_{CB} = -0.39$  V at pH 7.0),  
35 that the semiconductive material is expected to turn out fully degenerate and so to behave as a  
36  
37  
38  
39  
40  
41  
42  
43  
44  
45  
46  
47  
48  
49  
50  
51  
52  
53  
54  
55  
56  
57  
58  
59  
60



1  
2  
3 metal-like conductive film. Under this condition, the capacitive background current should  
4  
5 become theoretically constant and independent of the potential (because just governed by the  
6  
7 charging of the double-layer generated at the quasi-metallic EISA-SnO<sub>2</sub> film). This is however  
8  
9 not what we can observe in Figure 2 where the current density tends to slowly increase with the  
10  
11 rise of potential and even to become no more proportional to the scan rate at the highest cathodic  
12  
13 potentials. This behavior can be attributed to some faradaic contribution to the current, arising  
14  
15 most likely from slow proton intercalation as we have recently demonstrated to occur in TiO<sub>2</sub>  
16  
17 electrodes under similar buffered aqueous conditions.<sup>28</sup>  
18  
19  
20  
21  
22

23  
24 Whatever the reason for the lack of a constant capacitive background current at potential  
25  
26 values lower than  $E_{CB}$ , the good overlap of CVs normalized to  $v$  shown in Figure 2 for the  
27  
28 different EISA-SnO<sub>2</sub> electrodes unambiguously demonstrates that the electron transport  
29  
30 throughout the mesoporous network is not rate limiting within the range of scan rate investigated  
31  
32 (up to 1 V·s<sup>-1</sup>). In addition, the chemical capacitive current determined at -0.35 V is observed to  
33  
34 linearly scales with the film thickness (the current is 2.15 times larger at the 250-nm-thick EISA-  
35  
36 SnO<sub>2</sub> electrode than at the 100-nm-thick, see Figure 2), a result which tends to demonstrate that  
37  
38 the nanoporous film is structurally quite homogeneous normal to the underlying ITO surface.  
39  
40  
41  
42

43  
44 The above analysis of the capacitive current of EISA-SnO<sub>2</sub> electrodes finally allows us to define  
45  
46 the potential windows at pH 7.0 where the semiconductive film is switched from a poorly  
47  
48 conductive material to a metal-like conductive material with the applied potential (see Figure 2):  
49  
50

- 51 - for  $E > 0.2$  V, the SnO<sub>2</sub> semiconductive film remains insulating and the capacitance  
52  
53 arises exclusively from the underlying exposed conductive ITO interface;  
54  
55  
56  
57  
58  
59  
60

- for  $E_{CB} = -0.39 \text{ V} < E < 0.2 \text{ V}$ , the conductivity of the film is exponentially increased as the potential is downshifted by progressively filling the electronic states;
- for  $E < E_{CB}$ , the  $\text{SnO}_2$  film is fully degenerated and behaves as a high specific surface area quasi-metallic electrode.

It is worth to note that localized surface states originating from structural defects at the  $\text{SnO}_2$  surface are generally reported in the electronic description of mesoporous  $\text{SnO}_2$ -based electrodes.<sup>18</sup> It is commonly assumed that these surface states are energetically located below the conduction band, in an exponential distribution of localized states within the bandgap and also sometime characterized by a narrow distribution of monoenergetic electronic states leading to a small reversible capacitive peak located on CVs at the beginning of the transition from an insulating to conductive state. However, the capacitive current recorded with our EISA- $\text{SnO}_2$  electrodes does not allow to clearly identify such monoenergetic surface states, even though a small shoulder is visible at  $\sim 0.06 \text{ V}$  (vs.  $\text{Ag}/\text{AgCl}$ ) on the CVs of Figure 2 (especially for the 250-nm thick EISA- $\text{SnO}_2$  electrodes) as in other studies.<sup>16</sup>

### **Spectroelectrochemical characterization of EISA- $\text{SnO}_2$ films functionalized by redox-active chromophores.**

The 250-nm-thick EISA- $\text{SnO}_2$  electrodes were chemically functionalized by FMN and OsP (see Scheme S1 for molecular structures) through chemisorption of these compounds onto the metal oxide surface (on account of the presence of an organophosphorous anchoring group, the FMN and OsP compounds are able to strongly chemisorb onto the  $\text{SnO}_2$  surface through a similar heterocondensation reaction than that previously demonstrated at ITO surfaces<sup>29</sup>). These two molecules were selected because of (i) their intense redox-dependent visible absorption features

1  
2  
3 (ii) sufficiently different formal reduction potentials ( $E_{\text{FMN}}^{0'} = -0.4$  V and  $E_{\text{OsP}}^0 = 0.6$  V vs  
4 Ag/AgCl) so that in the case of FMN it lies close to the  $E_{\text{CB}}$  of SnO<sub>2</sub> while for OsP it locates at a  
5  
6 potential window where SnO<sub>2</sub> is insulating, and (iii) their ability to rapidly and reversibly  
7  
8 exchange electrons at a conductive interface.  
9  
10

11  
12  
13 After careful rinsing, the resulting modified electrodes were characterized by real-time UV-  
14  
15 visible absorption spectroelectrochemistry in a buffer solution. This methodology allows for  
16  
17 monitoring selectively the absorbance changes generated by an adsorbed redox-active  
18  
19 chromophore during the time course of a cyclic voltammetry experiment, leading thus to the  
20  
21 establishment of cyclic voltabsorptograms (CVAs) at specific wavelengths. Time derivative of  
22  
23 CVAs allows for derivative cyclic voltabsorptograms (DCVAs), which are equivalent to the  
24  
25 simultaneously recorded cyclic voltammograms but without the capacitive current contribution.<sup>30</sup>  
26  
27  
28 Consequently, CVAs and DCVAs allow for a more specific and accurate monitoring of electron  
29  
30 transfer reactions with adsorbed redox chromophores than CVs, for which the huge capacitive  
31  
32 contribution at negative potentials tends to mask the faradaic response.<sup>19</sup>  
33  
34  
35  
36  
37

38 During a CV scan, reduction/oxidation of the adsorbed redox chromophore can occur through  
39  
40 one or a combination of the following three electron transport mechanisms:  
41  
42  
43

44 (1) by physical diffusion of the redox probe throughout the void volume of the  
45  
46 mesoporous film up to the underlying conductive ITO electrode, a process that is however here  
47  
48 assumed to be unlikely on account of the strong chemisorption of redox chromophores we have  
49  
50 selected. The strong anchoring of FMN or OsP to the SnO<sub>2</sub> metal oxide surface was asserted by  
51  
52 the good stability of the resulting modified electrodes, even under prolonged immersion in a high  
53  
54  
55  
56  
57  
58  
59  
60

1  
2  
3 ionic strength aqueous buffer (desorption of the redox-active molecules has been observed to be  
4 less than 8% / hour);  
5  
6  
7

8  
9 (2) by a diffusion-like electron transport from the underlying conductive ITO electrode  
10 through electron hopping between adjacent redox probes, a phenomenon that is well-known in  
11 insulating films loaded with high surface coverages of redox-active molecules.<sup>31</sup>  
12  
13  
14

15  
16  
17 (3) by direct heterogeneous electron transfer at the SnO<sub>2</sub> interface when the Fermi level  
18 of electrons in the metal oxide film (or film conductivity) is raised sufficiently negative (i.e. by  
19 scanning the potential in CV at sufficiently cathodic values).  
20  
21  
22  
23

24  
25 A first set of experiments was conducted at pH 7.0 at a FMN-SnO<sub>2</sub> electrode by monitoring the  
26 current as well as the absorbance change at 450 nm during the time-course of a cyclic  
27 voltammogram performed from -0.1 to -0.6 V (vs. Ag/AgCl). As shown in Figure 3, the CV is  
28 characterized by a pair of well-defined symmetric waves centered at -0.4 V, a value that  
29 corresponds to the formal potential of the two-electrons redox transition of FMN at pH 7 in  
30 homogeneous solution.<sup>32,33</sup> The current intensity of the CVs is also proportional to the scan rate,  
31 up to  $\nu = 0.1 \text{ V}\cdot\text{s}^{-1}$  (Figure S4), characteristic of conductive surface-confined redox-active  
32 species. From integration of both cathodic and anodic peaks, a FMN surface coverage of ca. 0.6  
33 nmol·cm<sup>-2</sup> (normalized to the geometric electrode area) could be estimated when assuming a 2-  
34 electron redox transition. This value is consistent with that calculated from the absorbance  
35 change monitored at 450 nm on the CVA of Figure 3, assuming  $\Delta\epsilon_{450} \sim 10\,000 \text{ M}^{-1}\cdot\text{cm}^{-1}$ . The full  
36 reversibility and lack of hysteresis in the CVA is also coherent with the low  $\Delta E_p$  value observed  
37 on the CV ( $\Delta E_p < 30 \text{ mV}$ ), demonstrating that the reversible reduction of the chemisorbed FMN  
38 occurs under thermodynamic equilibrium within the range of scan rates investigated. The redox  
39  
40  
41  
42  
43  
44  
45  
46  
47  
48  
49  
50  
51  
52  
53  
54  
55  
56  
57  
58  
59  
60

1  
2  
3 behavior of FMN on SnO<sub>2</sub> is very similar to that reported on ITO,<sup>33</sup> a behavior which implies not  
4 only fast interfacial proton-coupled electron transfer reactions at the metal oxide interface, but  
5 also fast electron transport throughout the 250-nm-thick semiconductive SnO<sub>2</sub> network. This also  
6 entails that the EISA-SnO<sub>2</sub> electrode behaves as a metal-like electrode within the potential  
7 window corresponding to the FMN redox transition (Figure 3). A similar reversible electron  
8 transfer mechanism is also obtained for EISA-SnO<sub>2</sub> electrodes modified with microperoxidase  
9 11 (MP-11, Figure S5), a one-electron transfer redox chromophore characterized by a standard  
10 potential close to that of FMN ( $E_{\text{MP-11}}^0 = -0.37$  V) and that easily physisorbs within the  
11 mesoporous SnO<sub>2</sub> film (see Scheme S1). This result clearly shows that a reversible interfacial  
12 electron transfer can be expected as long as (i) the redox potential of the chemisorbed redox  
13 compound lies close or more negative to the conduction band potential of SnO<sub>2</sub> and (ii) the redox  
14 compound allows for a fast and reversible electron transfer reaction, independent of the nature of  
15 interactions the redox molecule has with the metal oxide surface. It is interesting to note that in  
16 contrast to the reversible wave we observed here for MP-11 in EISA-SnO<sub>2</sub>, an irreversible CV  
17 peak was previously reported for the same molecule in EISA-TiO<sub>2</sub> films.<sup>19</sup> This distinctive  
18 behavior is fully consistent with a conduction band potential of TiO<sub>2</sub> that is ~0.4 V more  
19 negative than SnO<sub>2</sub>.<sup>3</sup>

20  
21  
22  
23  
24  
25  
26  
27  
28  
29  
30  
31  
32  
33  
34  
35  
36  
37  
38  
39  
40  
41  
42  
43  
44 Similar experiments were next conducted at the OsP-functionalized SnO<sub>2</sub> electrodes. As the  
45 standard potential of the OsP complex ( $E_{\text{OsP}}^0 = 0.6$  V) lies in a potential window where SnO<sub>2</sub> is  
46 insulating, it can be anticipated that direct interfacial electron transfer between SnO<sub>2</sub> and OsP  
47 should proceed irreversibly once the potential applied to the SnO<sub>2</sub> film is sufficiently negative to  
48 convert the latter reasonably conductive (*i.e.* for  $E < 0.2$  V at pH 7). Since the osmium complex  
49 we have used to prepare the functionalized electrode was the reduced form, before performing  
50  
51  
52  
53  
54  
55  
56  
57  
58  
59  
60

1  
2  
3 any cathodic CV or CVA scan it was first necessary to in situ convert the chemisorbed complex  
4  
5 in its oxidized form. This has been rendered possible thanks to the application of a constant  
6  
7 preconditioning anodic potential ( $E = 1.0$  V) to the OsP-functionalized SnO<sub>2</sub> film for at least 30  
8  
9 seconds (see Figures S6). Under these conditions, even though the SnO<sub>2</sub> material remains  
10  
11 insulating, the electrochemical oxidation of the Os<sup>II</sup> complex is expected to proceed most likely  
12  
13 by a slow electron hopping between adjacent redox-active molecules. This slow oxidation  
14  
15 process is supported by the fact that the time needed to fully oxidize the chemisorbed OsP  
16  
17 complex contained within the 250-nm thick SnO<sub>2</sub> electrode (i.e. ~30 s) is relevant of an apparent  
18  
19 slow diffusion coefficient  $D$  of  $\sim 7 \times 10^{-12}$  cm<sup>2</sup>·s<sup>-1</sup> (assuming a diffusion length of  $l = (\pi Dt)^{1/2}$ ).  
20  
21 Such a low value is in agreement with a poorly efficient hopping electron transport between  
22  
23 adjacent adsorbed molecules. From the total absorbance change in Figure S6, a total surface  
24  
25 coverage  $\Gamma^0$  of 2.2 nmol·cm<sup>-2</sup> can be estimated for the grafted OsP complex (using an extinction  
26  
27 coefficient of 12000 M<sup>-1</sup>·cm<sup>-1</sup>, as usually reported for osmium tris-bipyridine complexes in  
28  
29 water).<sup>34</sup> This surface coverage (normalized to the geometric electrode area) is significantly  
30  
31 much larger than that obtained with the FMN chromophore, a difference that can be related to  
32  
33 the lower reactivity of phosphate compared to phosphonate anchoring groups toward  
34  
35 chemisorption on metal oxide surfaces.<sup>29</sup>  
36  
37  
38  
39  
40  
41  
42  
43  
44

45 Once converted to its oxidized form, the OsP-modified SnO<sub>2</sub> electrode was then characterized in  
46  
47 cyclic voltabsorptometry by monitoring the absorbance change at 485 nm. Resulting CVs and  
48  
49 CVAs are reported in Figure 3. Their shapes strongly differ from those obtained at the FMN-  
50  
51 functionalized SnO<sub>2</sub> electrode. Indeed, reduction of the Os<sup>III</sup> complex appears as a biphasic  
52  
53 process. A first reversible wave centered on the standard potential of the Os<sup>III</sup>/Os<sup>II</sup> redox couple  
54  
55 ( $E^0 = 0.6$  V) is observed at a potential where SnO<sub>2</sub> is insulating, leading to the reduction of a  
56  
57  
58  
59  
60

1  
2  
3 fraction of the total amount of adsorbed OsP complex (that only a fraction of OsP is reduced  
4 during this first reduction wave is clearly evident from the absorbance change as a function of  
5 potential, and it can be estimated to correspond to a fraction of ~50% at the scan rate of 0.05 V s<sup>-1</sup>  
6<sup>1</sup>). The remaining fraction of adsorbed OsP complex is thereafter fully reduced at more negative  
7 potential, leading to an irreversible reduction peak localized at 0.03 V. By comparing the CVs at  
8 different scan rates in figure S7, it can be concluded that the first reversible process is a  
9 diffusion-like process as its intensity is proportional to the square root of the scan rate. From the  
10 cathodic peak intensity of this reversible process, an apparent diffusion coefficient of ~10<sup>-11</sup>  
11 cm<sup>2</sup>·s<sup>-1</sup> can be estimated if assuming a starting volumic film concentration of 9 × 10<sup>-5</sup> mol·cm<sup>-3</sup>  
12 OsP within the 250-nm thick film (calculated from the geometric surface concentration of 2.2  
13 nmol cm<sup>-2</sup> OsP).  
14  
15  
16  
17  
18  
19  
20  
21  
22  
23  
24  
25  
26  
27  
28  
29  
30

31 This biphasic reduction process is reminiscent to that previously reported at mesoporous EISA-  
32 TiO<sub>2</sub> electrodes functionalized by an iron porphyrin.<sup>19</sup> It is indicative of the co-existence of two  
33 charge transfer mechanisms: a first diffusion-like mechanism involving most likely electron  
34 hopping transport between adjacent chemisorbed OsP complexes across the insulating SnO<sub>2</sub>  
35 network, and a second mechanism involving direct interfacial electron transfer from SnO<sub>2</sub> to the  
36 oxidized adsorbed molecule. This second mechanism is only efficient once a significant  
37 concentration of electrons is injected into the semiconductive material (i.e., at  $E < 0.2$  V at pH  
38 7.0).  
39  
40  
41  
42  
43  
44  
45  
46  
47  
48  
49

50 Quantitative analysis of this irreversible reduction process was performed on the derivative  
51 cyclic voltabsorptograms (DCVAs) recorded at different scan rates and pH, and represented as  
52 flux of molecules transformed ( $\Phi$  in mol·cm<sup>-2</sup>·s<sup>-1</sup>) as a function of potential using eq 2:  
53  
54  
55  
56  
57  
58  
59  
60

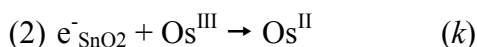
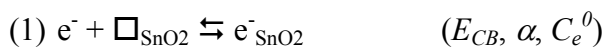
$$\phi = -\frac{1}{1000 \cdot \Delta \epsilon_{485}} \frac{v d A_{485}}{dE} \quad (2)$$

where  $\Delta \epsilon_{485}$  corresponds to the variation of the extinction coefficient between the two redox states of the osmium complex at 485 nm (i.e.,  $12000 \text{ mol}^{-1} \cdot \text{L} \cdot \text{cm}^{-1}$ ).

The experimental DCVAs recorded at pH 5 and different scan rates ranging from 10 to  $500 \text{ mV} \cdot \text{s}^{-1}$  are given in Figure 4 and S8 (only the forward cathodic scan is shown). It can be seen in Figure 4 that the amplitude of the total absorbance change is independent of the scan rate, indicating full redox conversion of the  $\text{Os}^{\text{III}}$  at the end of the forward cathodic scan whatever the scan rate, while the shapes of CVAs and DCVAs show strong dependence on the scan rate. At low scan rates, reduction of  $\text{Os}^{\text{III}}$  is a biphasic process as described above, and the two successive reduction peaks on the DCVA correspond to (i) a first reversible  $\text{Os}^{\text{III}}$  reduction through a diffusion-controlled process located within a potential window where  $\text{SnO}_2$  is insulating, followed by (ii) a second irreversible  $\text{Os}^{\text{III}}$  reduction through an interfacial electron transfer from  $\text{SnO}_2$  to the adsorbed complex at a potential where  $\text{SnO}_2$  is becoming increasingly conductive. As the scan rate is increased (and thus the time window of the CV decreased), the fraction of adsorbed  $\text{Os}^{\text{III}}$  reduced through the first diffusion mechanism is progressively decreased, while during the second irreversible electron transfer mechanism almost all of the remaining adsorbed  $\text{Os}^{\text{III}}$  molecules are reduced, even at the highest scan rates.

In order to get deeper insights into the heterogeneous electron transfer between  $\text{SnO}_2$  and the chemisorbed  $\text{Os}^{\text{III}}$  redox probe, the second irreversible wave was analyzed by assuming the following electron transfer/transport mechanism (same mechanism as previously proposed for  $\text{TiO}_2$ <sup>19</sup>):





The first equation is related to the fast electron injection from the underlying conductive ITO surface to an exponential distribution of electronic states of SnO<sub>2</sub> (i.e., a Boltzmann distribution of empty conduction band electronic states completed by the potential contribution of an exponential distribution of empty surface states localized in the bandgap), followed by fast transport of the injected electrons  $e^-_{\text{SnO}_2}$  through a random walk diffusion-like process across the SnO<sub>2</sub> mesoporous network (so fast that it can be assumed as being not rate limiting, see above).

In this description,  $C_e^0$  is the maximal concentration of electrons that can be injected at saturation in the SnO<sub>2</sub> material and the parameter  $\alpha$  is a dimensionless factor that characterizes the energy distribution of electronic states involved in the interfacial electron transfer. An  $\alpha$  value of 1 indicates that only electrons from the conduction band are involved in the heterogeneous electron transfer, while an  $\alpha$  value  $< 1$  indicates a significant contribution of the lower energy surface electronic states to the interfacial electron transfer.<sup>19</sup>

The second equation is related to the irreversible interfacial electron transfer reaction between the adsorbed Os<sup>III</sup> species and the electrons at the SnO<sub>2</sub> film/solution interface, wherein  $k$  is an average value of the interfacial electron transfer rates characterizing the different electronic states involved in the electron transfer. In the limiting case for which electron diffusion throughout the semi-conductive network is not interfering in the kinetics, the irreversible reduction wave can be described by the following analytical expression (see SI for details):

$$\phi = kC_e^0\Gamma \exp\left[-\alpha \frac{F}{RT}(E - E_{\text{CB}})\right] \exp\left(-\frac{RT}{\alpha F\nu} kC_e^0 \exp\left[-\alpha \frac{F}{RT}(E - E_{\text{CB}})\right]\right) \quad (3)$$

1  
2  
3 where  $E$  is the applied potential (in V),  $T$  the temperature (in K),  $F$  the Faraday constant (96500  
4 C·mol<sup>-1</sup>),  $R = 8.314 \text{ J}\cdot\text{K}^{-1}\cdot\text{mol}^{-1}$ , and  $\Gamma$  the surface coverage of the oxidized form of adsorbed  
5 redox chromophore directly reduced at the SnO<sub>2</sub> interface (in mol·cm<sup>-2</sup>). In the present case,  $\Gamma$  is  
6 function of the scan rate as partial reduction of the total amount of adsorbed Os<sup>III</sup>, i.e.  $\Gamma^0$ , can  
7 occur by an electron hopping when  $E$  is close to  $E^0_{\text{OsP}}$ . Consequently, we can define  $(1-f)$  the  
8 fraction of redox probe reduced during the first diffusion-controlled reduction step and  $f$  the  
9 fraction of Os<sup>III</sup> reduced during the second irreversible reduction step. The  $\Gamma$  value in eq 3 is thus  
10 given by the product  $f \times \Gamma^0$ .  
11  
12  
13  
14  
15  
16  
17  
18  
19  
20  
21  
22  
23

24 The analytical expression for the peak potential position of the irreversible wave is given by eq  
25 4:  
26  
27  
28  
29

$$E_P = E_{\text{CB}} + \frac{RT}{\alpha F} \ln \left( \frac{RT}{\alpha F} \frac{kC_e^0}{v} \right) \quad (4)$$

30  
31  
32  
33

34 The peak potential of the irreversible wave was shown to linearly vary with the logarithm of scan  
35 rate (Figure 5). From a linear regression fit of the experimental data and by assuming  $E_{\text{CB}} = -0.27$   
36 V at pH 5 using eq 1, values of  $\alpha = 0.71$  and  $kC_e^0 = 1.2 \times 10^5 \text{ s}^{-1}$  could be recovered. These  
37 parameters were then used in eq 3 to calculate the DCVAs at pH 5 in the range of 10 to  
38 500 mV·s<sup>-1</sup> (Figures 4 and S4). The fraction  $f$  of Os<sup>III</sup> reduced directly at the SnO<sub>2</sub> interface was  
39 fixed to adjust the intensity of the simulated irreversible wave.  
40  
41  
42  
43  
44  
45  
46  
47  
48

49 Similar experiments were also conducted at pH 7 and 8.5 using the same Os-SnO<sub>2</sub> electrode. The  
50 resulting DCVAs and CVs recorded at 0.05 V·s<sup>-1</sup> are plotted in Figure 5. As the pH was raised  
51 up, the irreversible wave was progressively shifted to lower potentials, consistent with the  
52 downshift of SnO<sub>2</sub> conduction band potential with the pH. The scan rate dependence of the peak  
53  
54  
55  
56  
57  
58  
59  
60

1  
2  
3 potential was analyzed according to eq 4, taking into account the pH-dependence of  $E_{CB}$   
4  
5 according to eq 1. The resulting data showed in Figure 5 overlay with that obtained at pH 5, and  
6  
7  
8 clearly demonstrate that  $\alpha$  as well as  $kC_e^0$  are almost unaffected by pH.  
9

10  
11 The very good fitting of eqs 3 and 4 to the experimental data demonstrates that our simple  
12  
13 model, initially developed for mesoporous EISA-TiO<sub>2</sub> electrodes,<sup>19</sup> can be extended to other  
14  
15 semi-conductive materials to extract the important parameters related to the interfacial electron  
16  
17 transfer between an adsorbed redox dye and the semi-conductive material. It has to be noticed  
18  
19 that in contrast to our previous work done with EISA-TiO<sub>2</sub>, the DCVA recorded up to 0.5 V·s<sup>-1</sup>  
20  
21 are not affected by ohmic drop. This is mainly due to the use of a higher ionic strength buffer  
22  
23 solution than previously, which is made possible thanks to the strong chemisorption of the  
24  
25 phosphonate osmium complex on SnO<sub>2</sub>, leading therefore to a high stability of the functionalized  
26  
27 electrodes toward desorption.  
28  
29  
30  
31  
32

33  
34 Some comments can be made on the two parameters  $\alpha$  and  $kC_e^0$  characterizing the interfacial  
35  
36 electron transfer between SnO<sub>2</sub> and the adsorbed Os<sup>III</sup> complex. First of all, the  $\alpha$  value of 0.71  
37  
38 indicates that the electrons involved in the interfacial electron transfer arise from a larger energy  
39  
40 distribution of electronic states than those of the conduction band, meaning thus that low-energy  
41  
42 electronic surface states distributed in the bandgap are involved in the interfacial electron  
43  
44 transfer. This result significantly differs from that we have previously obtained at EISA-TiO<sub>2</sub>  
45  
46 electrodes for which a  $\alpha$  value of 1 was found, characteristic of a heterogeneous electron transfer  
47  
48 reaction involving exclusively the extended conduction band states (Figure 6) but not the  
49  
50 electrons trapped in the low-energy states within the bandgap of TiO<sub>2</sub> (the latter can only be  
51  
52 indirectly involved through an equilibrated bulk trapping-detrapping mechanism with the  
53  
54  
55  
56  
57  
58  
59  
60

1  
2  
3 extended conduction band states).<sup>26</sup> An explanation we had put forward to interpret this lack of  
4  
5 electron transfer communication with localized traps in TiO<sub>2</sub> is that the traps are predominantly  
6  
7 located into the bulk of EISA-TiO<sub>2</sub> rather than on the surface of the metal oxide material.<sup>19</sup> In the  
8  
9 present case of EISA-SnO<sub>2</sub> electrodes, a  $\alpha$  value lower than one thus suggests that a significantly  
10  
11 higher number of surface traps are present, contributing thus to a wider energy range to the  
12  
13 interfacial electron transfer and so to an enlargement of the irreversible reduction peak in CV or  
14  
15 DCVA. These observations are in line with several reports highlighting the role of the surface  
16  
17 localized states in the faster recombination rates in dye-sensitized solar cells made of  
18  
19 nanoparticulate films of SnO<sub>2</sub> as compared to those made of TiO<sub>2</sub>.<sup>16-18</sup> In the present work, we  
20  
21 moreover demonstrate that the  $\alpha$  value is independent of the pH, a result which indicates that the  
22  
23 low-energy surface states distribution follow the same pH-dependence as for the conduction  
24  
25 band potential.  
26  
27  
28  
29  
30  
31

32  
33  
34 The second parameter  $kC_e^0$  describes an apparent first order interfacial electron transfer rate  
35  
36 wherein  $k$  corresponds in fact to an average value between the different electron transfer rates  
37  
38 arising from both the conduction band states and the localized surface states. Knowing the value  
39  
40 of  $C_e^0$  would allow extracting the average value  $k$  from  $kC_e^0$ , but because the information on the  
41  
42 density of electronic states and their distribution in the EISA-SnO<sub>2</sub> film is not available, this has  
43  
44 not been achieved. Interestingly,  $kC_e^0$  shows no significant dependence on pH, which most likely  
45  
46 indicates that the average value of  $k$  is almost pH-independent (if one assumes that  $C_e^0$  is  
47  
48 essentially a function of the intrinsic structural properties of the film). This result is reminiscent  
49  
50 of the observation made by Hupp *and coll.*, showing that electron transfer from the conduction  
51  
52 band of TiO<sub>2</sub> to a ruthenium complex is pH-independent over 19 pH unit range.<sup>35,36</sup> Such  
53  
54  
55  
56  
57  
58  
59  
60

1  
2  
3 independence of electron transfer rate with pH variation suggests that electron transfer at the  
4  
5 SnO<sub>2</sub> interface is decoupled from any proton transfer. While the potential of SnO<sub>2</sub> electronic  
6  
7 states is pH-dependent and that of the OsP redox couple is not, it is tempting to link the pH-  
8  
9 independent electron transfer rate to a pH-dependent driving force for the reaction by assuming  
10  
11 that the electron energy is equivalent to the conduction band energy. This assumption should  
12  
13 however only be valid for a proton-coupled interfacial electron transfer reaction, which is  
14  
15 apparently not the case in the present study on account of the pH-independence of the electron  
16  
17 transfer rate. Assuming here a pure electron transfer at the interface, it is therefore no more  
18  
19 possible to define the proper energy of the transferred electron as it is not defined by the pH-  
20  
21 dependent conduction band potential. The actual average driving force for interfacial electron  
22  
23 transfer from SnO<sub>2</sub> to a redox couple cannot be evaluated and thus remains an open question. As  
24  
25 a consequence it appears that more insights into the proton-coupled energetics of metal oxide  
26  
27 semiconductor electrodes are required to characterize electron transfer between such electrodes  
28  
29 and redox couples in terms of intrinsic parameters such as reorganization energies and pre-  
30  
31 exponential factors as in the Marcus-Gerischer equation.<sup>37</sup>  
32  
33  
34  
35  
36  
37  
38  
39  
40

## 41 CONCLUSION

42  
43  
44 In the present work, we prepared highly-ordered crystalline mesoporous SnO<sub>2</sub> electrodes by  
45  
46 EISA with large pores and adjustable thicknesses by taking advantage of the two deposition  
47  
48 regimes allowed by the dip-coating process. The thicker electrodes were then chemically  
49  
50 modified by two redox-active chromophores allowing us to investigate the heterogeneous  
51  
52 electron transfer at the SnO<sub>2</sub> interface to gain better insights into the reactive electronic states  
53  
54 involved. Quantitative analysis of the spectroelectrochemical results was achieved in the  
55  
56  
57  
58  
59  
60

1  
2  
3 theoretical framework initially developed for mesoporous  $\text{TiO}_2$  electrodes demonstrating thus  
4 that it can be successfully extended to other semi-conductive materials. Our results  
5 unambiguously evidence that the interfacial electron transfer at the  $\text{SnO}_2$  interface involves not  
6 only the extended conduction band states, but also the localized lower-energy electronic states  
7 present at the  $\text{SnO}_2$ /aqueous electrolyte interface. This significantly differs from our previous  
8 results at EISA- $\text{TiO}_2$  electrodes, wherein the interfacial electron transfer was shown to only  
9 involve the extended conduction band states. Accordingly, EISA- $\text{SnO}_2$  electrodes exhibit a  
10 specific interfacial electron-transfer reactivity related to the presence of sub-band gap surface  
11 states electronically-coupled to the adsorbed redox-active molecules.  
12  
13  
14  
15  
16  
17  
18  
19  
20  
21  
22  
23  
24  
25  
26  
27  
28  
29  
30  
31  
32  
33  
34  
35  
36  
37  
38  
39  
40  
41  
42  
43  
44  
45  
46  
47  
48  
49  
50  
51  
52  
53  
54  
55  
56  
57  
58  
59  
60

## ASSOCIATED CONTENT

**Supporting Information.** Details of the theoretical framework developed to analyze interfacial electron transfer at semi-conductive SnO<sub>2</sub> interface, Molecular structure of the redox probes, characterization of the EISA-SnO<sub>2</sub> electrodes prepared by thermo-ellipsometry, X-ray diffraction, gas adsorption/desorption. Complementary CVs, CVAs and DCVAs at modified EISA-SnO<sub>2</sub> electrodes.

## AUTHOR INFORMATION

**Corresponding Author**

[veronique.balland@univ-paris-diderot.fr](mailto:veronique.balland@univ-paris-diderot.fr)

**Author Contributions**

The manuscript was written through contributions of all authors. All authors have given approval to the final version of the manuscript.

**Acknowledgements**

This work was supported by the Agence Nationale pour la Recherche (ANR 3D-BIOELEC).

## REFERENCES

- (1) Alibabaei, L.; Luo, H.; House, R. L.; Hoertz, P. G.; Lopez, R.; Meyer, T. J. Applications of Metal Oxide Materials in Dye Sensitized Photoelectrosynthesis Cells for Making Solar Fuels: Let the Molecules Do the Work. *J. Mater. Chem. A* **2013**, *1*, 4133.
- (2) Wali, Q.; Fakharuddin, A.; Jose, R. Tin Oxide as a Photoanode For Dye-Sensitised Solar Cells: Current Progress and Future Challenges. *J. Power Sources* **2015**, *293*, 1039–1052.
- (3) Bolts, J. M.; Wrighton, M. S. Correlation of Photocurrent-Voltage Curves with Flat-Band Potential for Stable Photoelectrodes for the Photoelectrolysis of Water. *J. Phys. Chem.* **1976**, *80*, 2641–2645.
- (4) Green, A. N. M.; Palomares, E.; Haque, S. A.; Kroon, J. M.; Durrant, J. R. Charge

- 1  
2  
3 Transport versus Recombination in Dye-Sensitized Solar Cells Employing  
4 Nanocrystalline TiO<sub>2</sub> and SnO<sub>2</sub> Films. *J. Phys. Chem. B* **2005**, *109*, 12525–12533.
- 5  
6 (5) Zhang, M.; Chen, C.; Ma, W.; Zhao, J. Visible-Light-Induced Aerobic Oxidation of  
7 Alcohols in a Coupled Photocatalytic System of Dye-Sensitized TiO<sub>2</sub> and TEMPO.  
8 *Angew. Chemie* **2008**, *120*, 9876–9879.
- 9  
10 (6) Song, W.; Vannucci, A. K.; Farnum, B. H.; Lapides, A. M.; Brennaman, M. K.; Kalanyan,  
11 B.; Alibabaei, L.; Concepcion, J. J.; Losego, M. D.; Parsons, G. N. et al. Visible Light  
12 Driven Benzyl Alcohol Dehydrogenation in a Dye-Sensitized Photoelectrosynthesis Cell.  
13 *J. Am. Chem. Soc.* **2014**, *136*, 9773–9779.
- 14  
15 (7) Milot, R. L.; Moore, G. F.; Crabtree, R. H.; Brudvig, G. W.; Schmittenmaer, C. A.  
16 Electron Injection Dynamics from Photoexcited Porphyrin Dyes into SnO<sub>2</sub> and TiO<sub>2</sub>  
17 Nanoparticles. *J. Phys. Chem. C* **2013**, *117*, 21662–21670.
- 18  
19 (8) Milot, R. L.; Schmittenmaer, C. A. Electron Injection Dynamics in High-Potential  
20 Porphyrin Photoanodes. *Acc. Chem. Res.* **2015**, *48*, 1423–1341.
- 21  
22 (9) Tiwana, P.; Docampo, P.; Johnston, M. B.; Snaith, H. J.; Herz, L. M. Electron Mobility  
23 and Injection Dynamics in Mesoporous ZnO, SnO<sub>2</sub>, and TiO<sub>2</sub> Films Used in Dye-  
24 Sensitized Solar Cells. *ACS Nano* **2011**, *5*, 5158–5166.
- 25  
26 (10) Kamat, P. V.; Bedja, I.; Hotchandani, S.; Patterson, L. K. Photosensitization of  
27 Nanocrystalline Semiconductor Films. Modulation of Electron Transfer between Excited  
28 Ruthenium Complex and SnO<sub>2</sub> Nanocrystallites with an Externally Applied Bias. *J. Phys.*  
29 *Chem.* **1996**, *100*, 4900–4908.
- 30  
31 (11) Huang, J.; Stockwell, D.; Boulesbaa, A.; Guo, J.; Lian, T. Comparison of Electron  
32 Injection Dynamics from Rhodamine B to In<sub>2</sub>O<sub>3</sub>, SnO<sub>2</sub>, and ZnO Nanocrystalline Thin  
33 Films. *J. Phys. Chem. C* **2008**, *112*, 5203–5212.
- 34  
35 (12) Godin, R.; Sherman, B. D.; Bergkamp, J. J.; Chesta, C. A.; Moore, A. L.; Moore, T. A.;  
36 Palacios, R. E.; Cosa, G. Charge-Transfer Dynamics of Fluorescent Dye-Sensitized  
37 Electrodes under Applied Biases. *J. Phys. Chem. Lett.* **2015**, *6*, 2688–2693.
- 38  
39 (13) Asbury, J. B.; Hao, E.; Wang, Y.; Ghosh, H. N.; Lian, T. Ultrafast Electron Transfer  
40 Dynamics from Molecular Adsorbates to Semiconductor Nanocrystalline Films. **2001**,  
41 *105*, 4545.
- 42  
43 (14) Anderson, N. A.; Lian, T. Ultrafast Electron Transfer At the Molecule-Semiconductor  
44 Nanoparticle Interface. *Annu. Rev. Phys. Chem.* **2005**, *56*, 491–519.
- 45  
46 (15) Bergeron, B. V.; Marton, A.; Oskam, G.; Meyer, G. J. Dye-Sensitized SnO<sub>2</sub> Electrodes  
47 with Iodide and Pseudohalide Redox Mediators. *J. Phys. Chem. B* **2005**, *109*, 937–43.
- 48  
49 (16) Knauf, R. R.; Brennaman, M. K.; Alibabaei, L.; Norris, M. R.; Dempsey, J. L. Revealing  
50 the Relationship between Semiconductor Electronic Structure and Electron Transfer  
51 Dynamics at Metal Oxide–Chromophore Interfaces. *J. Phys. Chem. C* **2013**, *117*, 25259–  
52 25268.
- 53  
54 (17) Prasittichai, C.; Hupp, J. T. Surface Modification of SnO<sub>2</sub> Photoelectrodes in Dye-  
55 Sensitized Solar Cells: Significant Improvements in Photovoltage via Al<sub>2</sub>O<sub>3</sub> Atomic Layer  
56  
57  
58  
59  
60



- 1  
2  
3 Deposition. *J. Phys. Chem. Lett.* **2010**, *1*, 1611–1615.
- 4  
5 (18) Huang, Q.; Li, F.; Gong, Y.; Luo, J. Recombination in SnO<sub>2</sub>-Based Quantum Dots  
6 Sensitized Solar Cells: The Role of Surface States. *J. Phys. Chem. C* **2013**, *2*–10.  
7
- 8 (19) Renault, C.; Nicole, L.; Sanchez, C.; Costentin, C.; Balland, V.; Limoges, B. Unraveling  
9 the Charge Transfer/Electron Transport in Mesoporous Semiconductive TiO<sub>2</sub> Films by  
10 Voltabsorptometry. *Phys. Chem. Chem. Phys.* **2015**, *17*, 10592–10607.  
11
- 12 (20) Sakatani, Y.; Grosso, D.; Nicole, L.; Boissiere, C.; de A. A. Soler-Illia, G. J.; Sanchez, C.  
13 Optimised Photocatalytic Activity of Grid-like Mesoporous TiO<sub>2</sub> Films: Effect of  
14 Crystallinity, Pore Size Distribution, and Pore Accessibility. *J. Mater. Chem.* **2006**, *16*,  
15 77–82.  
16
- 17 (21) Brezesinski, T.; Fischer, A.; Iimura, K. I.; Sanchez, C.; Grosso, D.; Antonietti, M.;  
18 Smarsly, B. M. Generation of Self-Assembled 3D Mesostructured SnO<sub>2</sub> Thin Films with  
19 Highly Crystalline Frameworks. *Adv. Funct. Mater.* **2006**, *16*, 1433–1440.  
20
- 21 (22) Grosso, D. How to Exploit the Full Potential of the Dip-Coating Process to Better Control  
22 Film Formation. *J. Mater. Chem.* **2011**, *21*, 17033.  
23
- 24 (23) Gillaizeau-Gauthier, I.; Odobel, F.; Alebbi, M.; Argazzi, R.; Costa, E.; Bignozzi, C. A.;  
25 Qu, P.; Meyer, G. J. Phosphonate-Based Bipyridine Dyes for Stable Photovoltaic Devices.  
26 *Inorg. Chem.* **2001**, *40*, 6073–6079.  
27
- 28 (24) Lepoutre, S.; Smått, J.-H.; Laberty, C.; Amenitsch, H.; Grosso, D.; Lindén, M. Detailed  
29 Study of the Pore-Filling Processes during Nanocasting of Mesoporous Films using  
30 SnO<sub>2</sub>/SiO<sub>2</sub> as a Model System. *Microporous Mesoporous Mater.* **2009**, *123*, 185–192.  
31
- 32 (25) Boissiere, C.; Grosso, D.; Lepoutre, S.; Nicole, L.; Bruneau, A. B.; Sanchez, C. Porosity  
33 and Mechanical Properties of Mesoporous Thin Films Assessed by Environmental  
34 Ellipsometric Porosimetry. *Langmuir* **2005**, *21*, 12362–12371.  
35
- 36 (26) Fabregat-Santiago, F.; Mora-Seró, I.; Garcia-Belmonte, G.; Bisquert, J. Cyclic  
37 Voltammetry Studies of Nanoporous Semiconductors. Capacitive and Reactive Properties  
38 of Nanocrystalline TiO<sub>2</sub> Electrodes in Aqueous Electrolyte. *J. Phys. Chem. B* **2003**, *107*,  
39 758–768.  
40
- 41 (27) Berger, T.; Monllor-Satoca, D.; Jankulovska, M.; Lana-Villarreal, T.; Gomez, R. The  
42 Electrochemistry of Nanostructured Titanium Dioxide Electrodes. *ChemPhysChem* **2012**,  
43 *13*, 2824–2875.  
44
- 45 (28) Kim, Y.-S.; Kriegel, S.; Harris, K. D.; Costentin, C.; Limoges, B.; Balland, V. Evidencing  
46 Fast, Massive, and Reversible H<sup>+</sup> Insertion in Nanostructured TiO<sub>2</sub> Electrodes at Neutral  
47 pH. Where Do Protons Come From? *J. Phys. Chem. C* **2017**, *121*, 10325–10335.  
48
- 49 (29) Forget, A.; Limoges, B.; Balland, V. Efficient Chemisorption of Organophosphorous  
50 Redox Probes on Indium Tin Oxide Surfaces under Mild Conditions. *Langmuir* **2015**, *31*,  
51 1931–1940.  
52
- 53 (30) Bancroft, E. E.; Sidwell, J. S.; Blount, H. N. Derivative Linear Sweep and Derivative  
54 Cyclic Voltabsorptometry. *Anal. Chem.* **1981**, *53*, 1390–1394.  
55  
56  
57  
58  
59  
60

- 1  
2  
3  
4  
5  
6  
7  
8  
9  
10  
11  
12  
13  
14  
15  
16  
17  
18  
19  
20  
21  
22  
23  
24  
25  
26  
27  
28  
29  
30  
31  
32  
33  
34  
35  
36  
37  
38  
39  
40  
41  
42  
43  
44  
45  
46  
47  
48  
49  
50  
51  
52  
53  
54  
55  
56  
57  
58  
59  
60
- (31) Trammell, S. A.; Meyer, T. J. Diffusional Mediation of Surface Electron Transfer on TiO<sub>2</sub>. *J. Phys. Chem. B* **1999**, *103*, 104–107.
- (32) Mayhew, S. G. The Effects of pH and Semiquinone Formation on the Oxidation–Reduction Potentials of Flavin Mononucleotide. *Eur. J. Biochem.* **1999**, *265*, 698–702.
- (33) Forget, A.; Tucker, R. T.; Brett, M. J.; Limoges, B.; Balland, V. Tuning the Reactivity of Nanostructured Indium Tin Oxide Electrodes Toward Chemisorption. *Chem. Commun.* **2015**, *51*, 6944–6947.
- (34) Jung, M. C.; Munro, N.; Shi, G.; Michael, A. C.; Weber, S. G. Use of Tris(2,2′-bipyridine)osmium as a Photoluminescence-Following Electron-Transfer Reagent for Postcolumn Detection in Capillary High-Performance Liquid Chromatography. *Anal. Chem.* **2006**, *78*, 1761–1768.
- (35) Yan, S. G.; Hupp, J. T. Semiconductor-Based Interfacial Electron-Transfer Reactivity: Decoupling Kinetics from pH-Dependent Band Energetics in a Dye-Sensitized Titanium Dioxide/Aqueous Solution System. *J. Phys. Chem.* **1996**, *100*, 6867–6870.
- (36) Yan, S. G.; Hupp, J. T. Energetics of Electron Transfer at the Nanocrystalline Titanium Dioxide Semiconductor/Aqueous Solution Interface: pH Invariance of the Metal-Based Formal Potential of a Representative Surface-Attached Dye Couple. *J. Phys. Chem. B* **1997**, *101*, 1493–1495.
- (37) Gerischer, H. The Impact of Semiconductors on the Concepts of Electrochemistry. *Electrochim. Acta* **1990**, *35*, 1677–1699.

## FIGURES

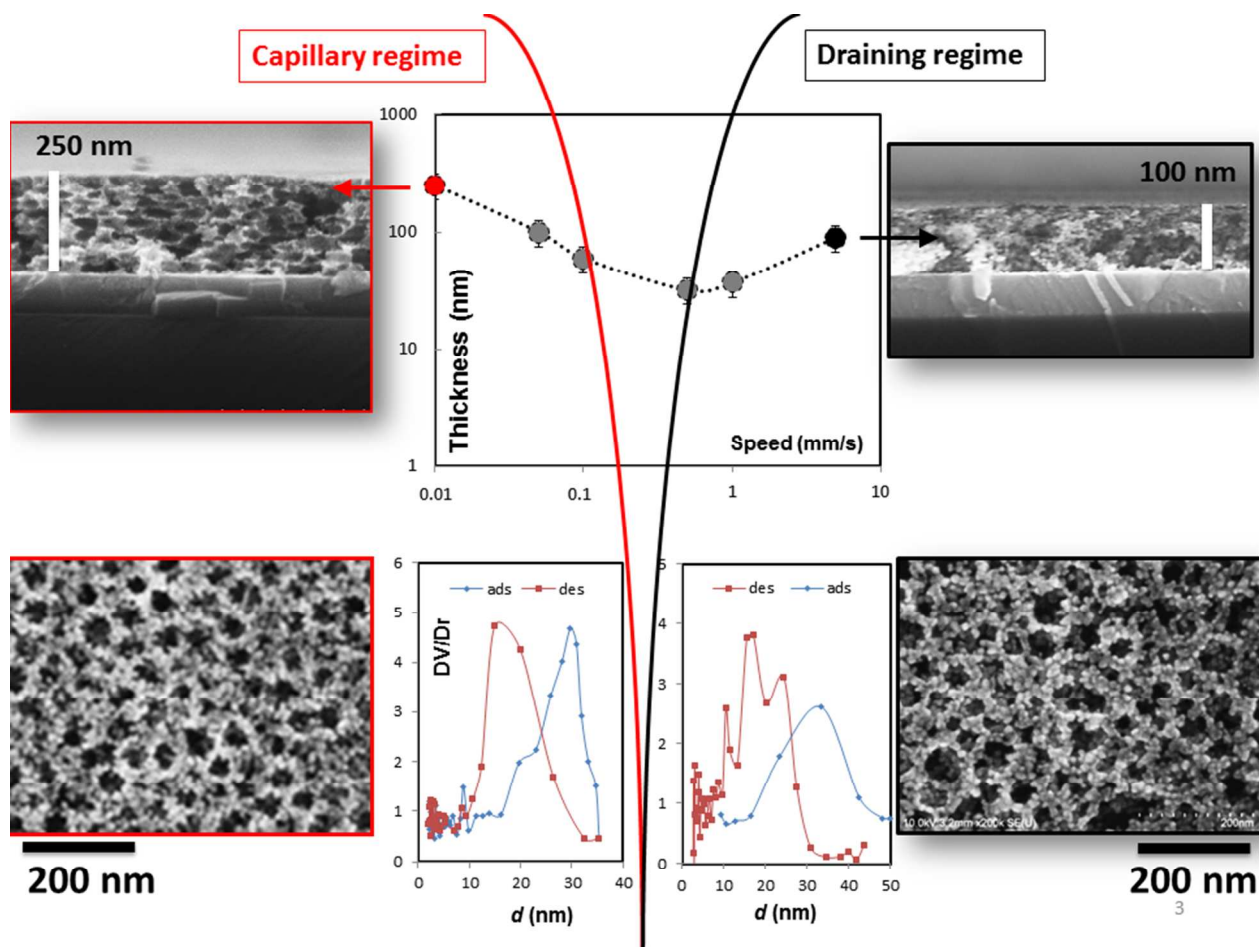


**Figure 1.** Cross-sectional and top SEM-FEG images of the SnO<sub>2</sub>-films prepared at (left) 0.01 and (right) 5 mm·s<sup>-1</sup>. Middle up: film thickness (determined by ellipsometry) as a function of the dip-coating withdrawal speed. Middle down: pore size distributions calculated from adsorption/desorption isotherms.

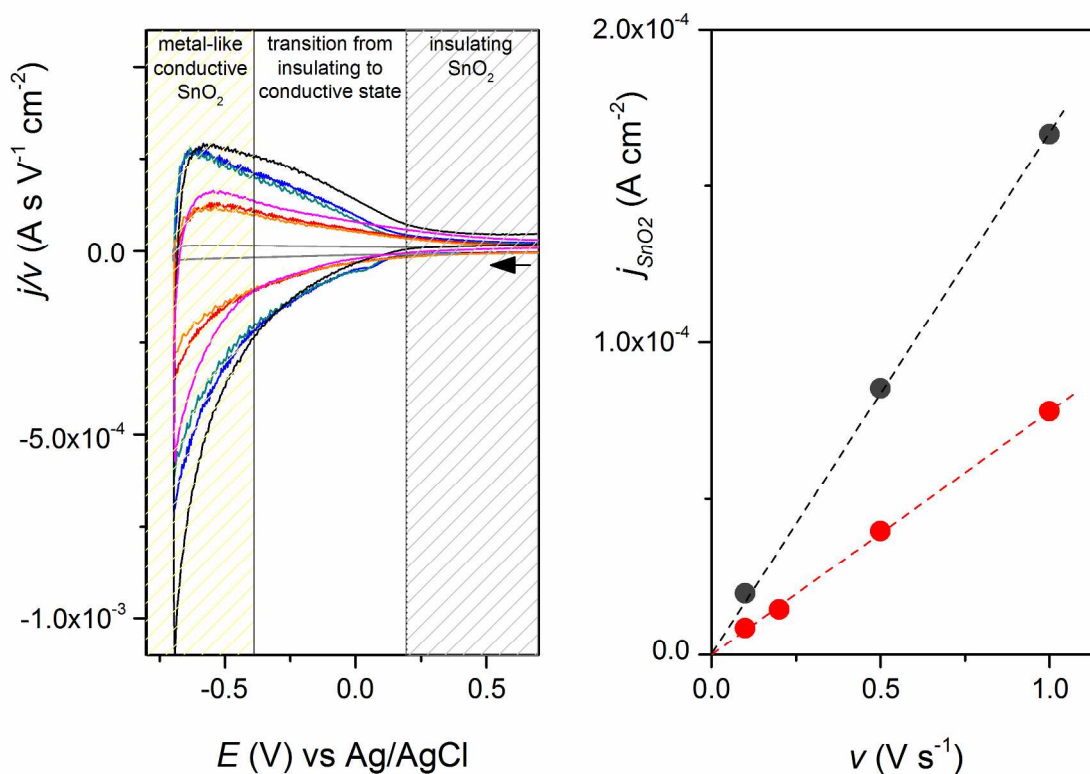


**Figure 2.** Left: scan rate-normalized cyclic voltammograms at (grey line) a planar ITO electrode, (magenta, red, and orange curves) a 100-nm-thick EISA- $\text{SnO}_2$  electrode, and (black, blue, and green curves) a 250-nm-thick EISA- $\text{SnO}_2$  electrode in a Hepes aqueous buffer solution of pH 7. The three tested scan rates for each EISA- $\text{SnO}_2$  electrode were respectively of 0.1, 0.5 and  $1 \text{ V}\cdot\text{s}^{-1}$ . Right: current density determined at  $-0.35 \text{ V}$  (corrected from the capacitive contribution of the underlying conductive ITO) as a function of the scan rate for the (red) 100- and (black) 250-nm EISA- $\text{SnO}_2$  electrode. Dashed lines correspond to the linear regression fits with slopes of  $7.8 \times 10^{-5}$  and  $16.75 \times 10^{-5} \text{ A}\cdot\text{s}\cdot\text{V}^{-1}\cdot\text{cm}^{-2}$  for the 100- and 250-nm EISA- $\text{SnO}_2$  film, respectively.

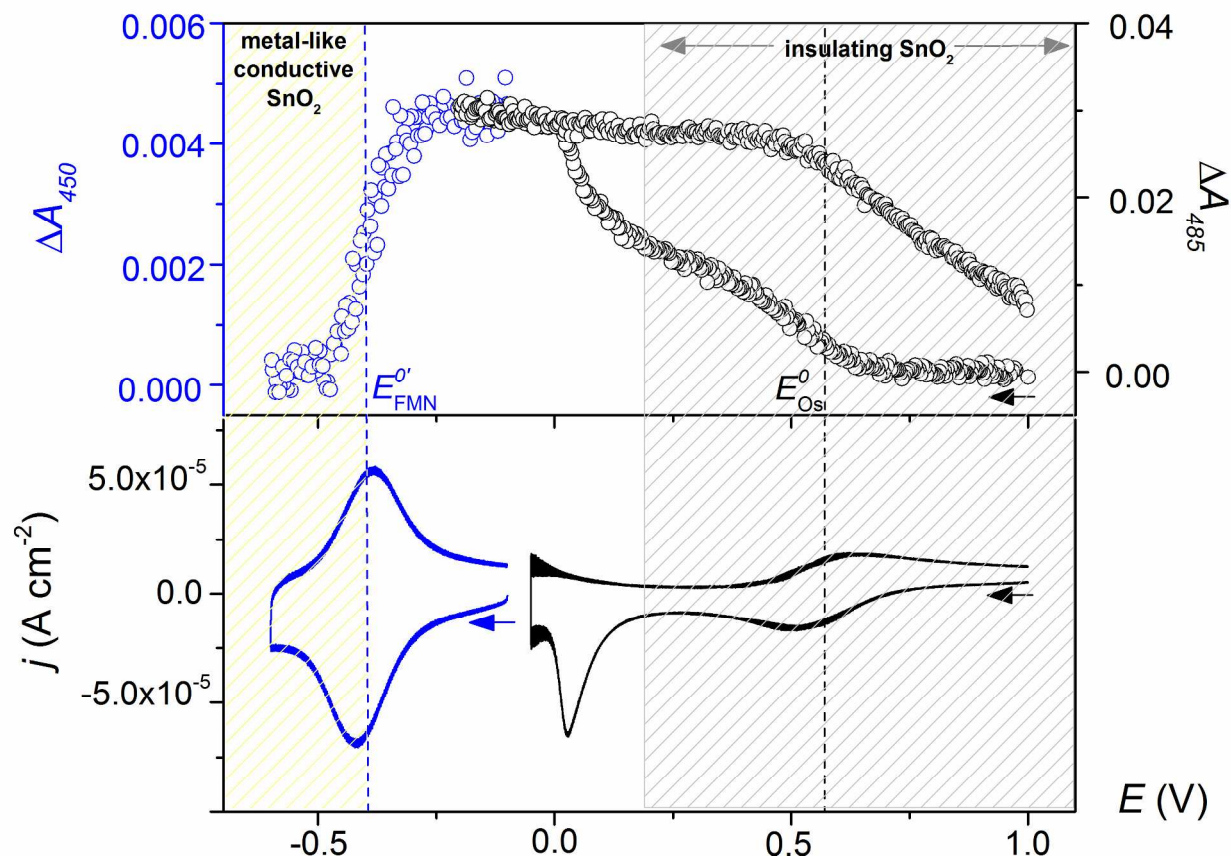


**Figure 3.** (Top) cyclic voltabsorptograms and (down) cyclic voltammograms recorded ( $\nu = 0.05$  V·s<sup>-1</sup>) at a (blue) FMN- and (black) OsP-modified EISA-SnO<sub>2</sub> electrode (250 nm-thick) in a Hepes buffer (pH 7). For the CVAs, the FMN and the osmium complex were monitored at 450 nm and 485 nm, respectively. The dashed lines indicate the formal reduction potential of each redox probe in solution at pH 7.

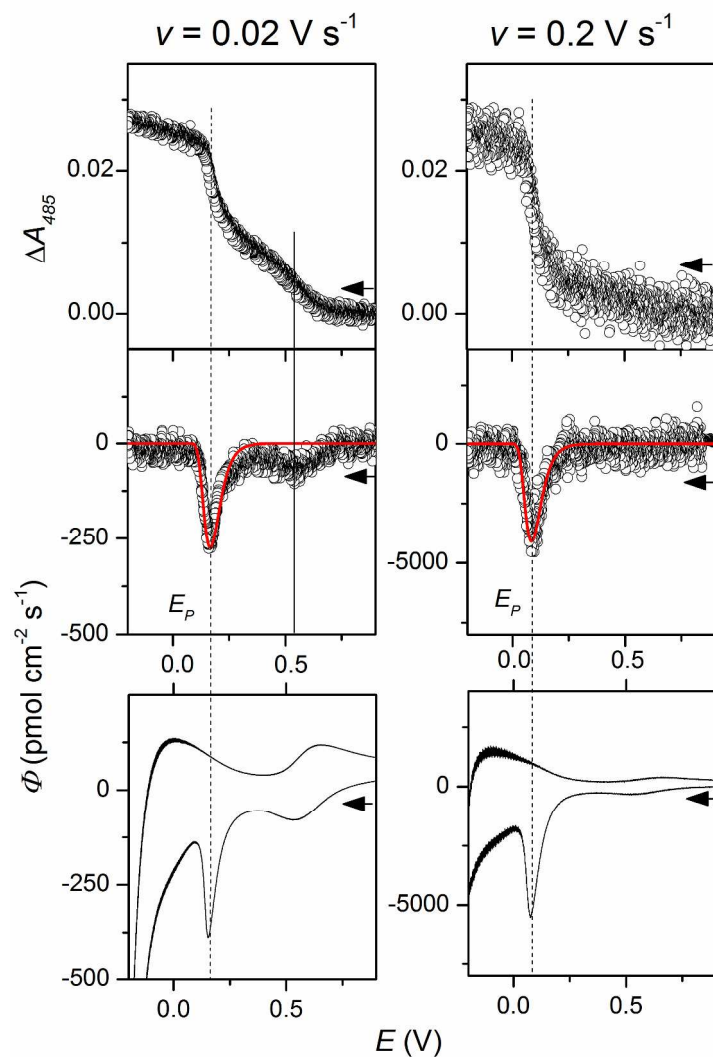


**Figure 4.** (Top) cathodic linear voltabsorptograms, (down) cyclic voltammograms, and (middle) cathodic derivative linear voltabsorptograms monitored at 485 nm at 0.02 or 0.2 V·s<sup>-1</sup> at a OsP-modified EISA-SnO<sub>2</sub> electrode in a Mes buffer of pH 5 (T = 20°C,  $\Gamma^0 = 2.2 \text{ nmol}\cdot\text{cm}^{-2}$ ). Red lines: fits of eq 3 to the experimental plots using  $E_{CB} = -0.27 \text{ V}$ ,  $\alpha = 0.71$ ,  $kC_e^0 = 1.2 \cdot 10^5 \text{ s}^{-1}$ , and  $f = 0.6$  at 0.02 V·s<sup>-1</sup> and  $f = 0.95$  at 0.2 V·s<sup>-1</sup>.

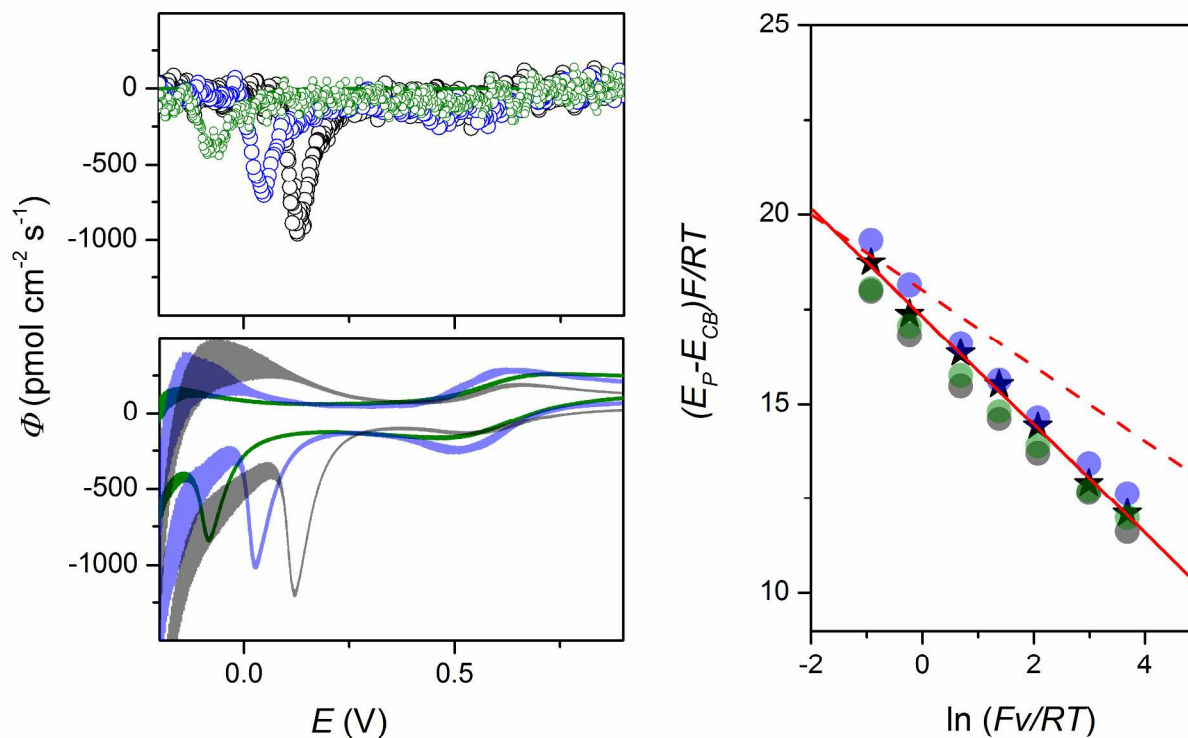


**Figure 5.** Left: DCVAs (top) and CVs (down) recorded at  $\nu = 0.05 \text{ V}\cdot\text{s}^{-1}$  at a OsP-modified EISA-SnO<sub>2</sub> electrode in an aqueous buffer at pH 5 (grey), 7 (blue) and 8.5 (green). Right: plot of the irreversible peak potential value obtained from CVs (●) or DCVAs (★) at pH 5 (green), 7 (blue) and 8.5 (grey) as a function of the scan rate, assuming  $E_{CB} = -0.27 \text{ V}$ ,  $-0.39 \text{ V}$  and  $-0.48 \text{ V}$  at pH 5, 7 and 8.5, respectively (see eq 1). Plain red line: linear regression fit of eq 4 to the experimental data obtained from the DCVAs at pH 5 leading to  $\alpha = 0.71$  and  $kC_e^0 = 1.2 \times 10^5 \text{ s}^{-1}$ . Dashed red line: example of linear dependence with  $\alpha = 1$ .

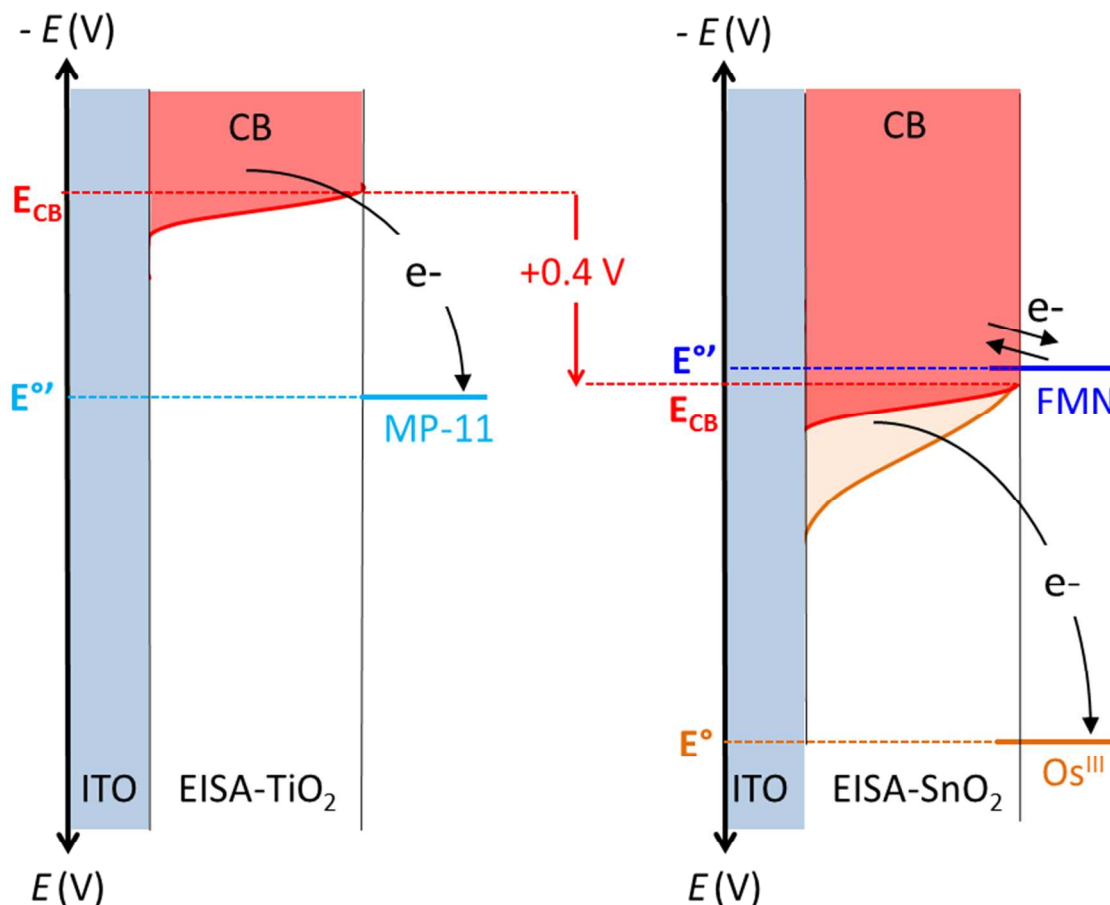


**Figure 6.** Schematic representations of the distribution of electronic states involved in the interfacial electron transfer between (left) EISA-TiO<sub>2</sub> and (right) EISA-SnO<sub>2</sub> semiconductive film electrodes and different adsorbed redox probes. In the case of the EISA-TiO<sub>2</sub> electrode, only electrons arising from the conduction band (Boltzmann distribution) are involved in the interfacial electron transfer, while for the EISA-SnO<sub>2</sub> electrode, low-energy electronic states localized in the band gap (exponential distribution with  $\alpha < 1$ ) also contribute to the interfacial electron transfer.



TABLES.

**Table 1.** Key morphological parameters of EISA-SnO<sub>2</sub> films determined by ellipsometry.

Template	Withdrawal speed (mm·s <sup>-1</sup> )	Thickness (nm)	Porosity (%)	Pore Size IEP (nm)	Ref
PIB-b-PEO	0.01	250-300	65-70	20-30	This work
PIB-b-PEO	5	80-100	65-70	20-30	This work
KLE	6	110	45,5	7 × 14 <sup>§</sup>	<sup>21</sup>

<sup>§</sup> Ellipsoidal pores

## Table of Contents Graphic

